5-2015

# Phased Array Beamsteering in Composite Laminates for Guided Wave Structural Health Monitoring

Peter Osterc

# PHASED ARRAY BEAMSTEERING IN COMPOSITE LAMINATES FOR GUIDED WAVE STRUCTURAL HEALTH MONITORING

A Thesis

Submitted to the Faculty

of

Embry-Riddle Aeronautical University

by

Peter Osterc

In Partial Fulfillment of the

Requirements for the Degree

of

Master of Science in Aerospace Engineering

May 2015

Embry-Riddle Aeronautical University

Daytona Beach, Florida

PHASED ARRAY BEAMSTEERING IN COMPOSITE LAMINATES
FOR GUIDED WAVE STRUCTURAL HEALTH MONITORING

by

Peter Osterc

A Thesis prepared under the direction of the candidate's committee chairman, Dr. Daewon Kim, Department of Aerospace Engineering, and has been approved by the members of the thesis committee. It was submitted to the School of Graduate Studies and Research and was accepted in partial fulfillment of the requirements for the degree of Master of Science in Aerospace Engineering

THESIS COMMITTEE

Chairman, Dr. Daewon Kim

Member, Dr. Namilae Sirish

Member, Dr. Jeff Brown

Department Chair, Dr. Anastasios Lyrintzis
or Graduate Program Coordinator, Dr. Yi Zhao

4/24/2015
Date

Dean of College of Engineering, Dr. Maj Mirmirani

4/24/2015
Date

Associate VP for Academics, Dr. Robert Oxley

4-27-2015
Date

# ACKNOWLEDGMENTS

I would like to thank my thesis supervisor, Dr. Daewon Kim, for giving me the opportunity to pursue my thesis work. His guidance, understanding and encouragement throughout the research process have been immeasurable.

Further, I would also like to thank the rest of the committee members, Dr. Jeff Brown and Dr. Namilae Sirish. Their advice and suggestions are greatly appreciated.

I would also like to thank my friends and colleagues in the research group. Audrey Gbaguidi and David Tan for their help and suggestions in implementing numerical methods and Balaji Sivasubramanian and Sai Harsha for their assistance in setting up and performing the experimental work.

Finally, I would like to thank my family for their continuous support throughout my studies.

TABLE OF CONTENTS

# LIST OF TABLES

# LIST OF FIGURES

# ABSTRACT

Osterc, Peter MSAE, Embry-Riddle Aeronautical University, May 2015. Phased Array Beamsteering in Composite Laminates for Guided Wave Structural Health Monitoring.

In this study a guided wave phased array beamsteering approach is applied to composite laminates. Current beamsteering algorithms derived for isotropic materials assume omnidirectional wave propagation. Due to inherent anisotropy in composites, guided wave propagation varies with direction and wavefronts no longer have perfect circular shapes.

By examining slowness, velocity and wave curves, as well as amplitude variation with direction for a given composite laminate, the wavefront from a single source can be described as a function of the angle of propagation and distance from origin. Using this approach, a more general delay and sum beamforming algorithm for composite laminates is developed for any desired wave mode.

It is shown that anisotropic wave mode shapes can be effectively used for beamsteering in certain directions with a linear array and performance similar or even better than the isotropic case. However, the useful range of angles with a 1-D linear array for anisotropic wave modes is quite small and other directions exhibit undesired grating lobes and large sidelobes.

Results from the modified beamforming algorithm are also compared and validated with Finite Element Model simulations. Good agreement is shown between analytical predictions and finite element results.

Experimental validation is performed using an aluminum and composite plate and linear arrays of piezoelectric actuators for guided wave excitation. Successful beamforming is shown in the experimental study based on the algorithm predictions.

# 1. Introduction

With ever more extensive use of composites in various industries, especially mechanical and aerospace structures, damage detection and evaluation is becoming increasingly important.

Damage in composite materials can occur through multiple mechanisms. Time dependent fatigue and propagation of damage in composites due to impacts, which may not be visible as surface damage, can often cause delamination of the underlying layers. Since propagation or occurrence of damage is not nearly as well known and possible to visually identify as in metals, other means of detecting damage are needed.

Conventional nondestructive evaluation (NDE) techniques which are commonly used in monitoring metallic structures have been successfully applied to composite structures; however, such testing is very limited in area and thus too time and labor-consuming across large areas and also not applicable to certain complex geometries.

For plate-like structures, structural health monitoring (SHM) using phased array beamsteering of guided Lamb waves is a promising approach to damage detection and evaluation. This approach will be further discussed throughout this thesis.

## 1.1 Structural Health Monitoring

Active structural health monitoring, where sensors are embedded and autonomously evaluating the structure in real-time during usage, is becoming more and more popular for the many benefits it can provide. Amongst these are increased structure reliability, accident prevention, prediction of remaining useful life of the structure which can be utilized for condition-based-maintenance and many other derived benefits.

An active SHM approach would potentially provide an automated system for monitoring composite structures, with the ability to detect and locate damage immediately as it occurs. There are several different methods that exist for SHM and/or NDE which include but are not limited to fiber optic sensors, electrical impedance, acoustic emissions, microelectromechanical systems (MEMS) accelerometers, and ultrasonics.

Ultrasonics and radiography introduce energy into the structure to observe the response using piezoelectric transducers and x-rays. NDE techniques often use through-thickness evaluation. However, for SHM systems, guided lamb waves that propagate in the plane of the plate structures are of greater interest.

Many current SHM systems utilize Lamb waves to detect damage both in metallic and composite structures. Lamb waves in any material have the great advantage of propagating across long distances with only a small loss of amplitude (Rose, 1999). This means that a large area can be monitored with just a few sensors. In contrast to conventional NDE techniques, damage can be detected even when not in the vicinity of the sensors.

Guided lamb waves can be excited and sensed in many different ways. Piezoceramic (PZT) and MacroFiber Composites (MFC) actuators, fiber optics, EMATs, Magnetostrictive sensors, AFC, SMART layers etc. have all been studied and used by researchers. PZT actuators and those similar to them are particularly promising since they can act as both actuators and sensors. Thus the number of parts can be reduced, and a whole structure can be monitored by a minimum number of actuators. Various arrangements of sensors have been proposed and experimentally studied by researchers. An overview of many recent approaches is given by Lissenden and Rose (2008). A promising system is beamsteering using a central phased array of actuators and is the focus of the work described in this thesis as well.

## 1.2 Guided Lamb Waves

Guided Lamb waves are elastic waves that exist in thin, plate-like structures, where thickness is at least an order of magnitude smaller than other dimensions. Lamb waves in any solid media are highly dispersive, e.g. the wave velocity is a function of frequency. Furthermore, a given structure can theoretically support an infinite number of different Lamb wave modes. The modes can generally be grouped into two distinct types of Lamb waves: symmetric (extensional) and antisymmetric (flexural).

Dispersion curves describe the relation between frequency and phase or group velocity for the different modes. Dispersion for isotropic plates is only a function of material properties and governing relations are quite straightforward to derive from

3D elasticity theory. Solutions for valid wave modes however can only be obtained using numerical methods (Rose, 1999). For anisotropic materials, dispersion properties become direction dependent as well and can generally not be assumed to be constant in every direction.

Despite added complications, the dispersion relations for composite materials can be solved numerically from equations of motion and 3D elasticity or through higher order plate theory as shown by Wang and Yuan (2007a). They can also be determined experimentally (Valdes & Soutis, 2002) or through finite element methods (Wang & Yuan, 2006).

### 1.3 Phased array Beamforming

Phased array beamforming is a technique used in different fields for directional signal sending or reception. It utilizes multiple actuators to form a focused beam. For an SHM application, this enables determining the exact direction of the damage in relation to the sensor/actuator array. With just around 4-10 actuators, a focused beam can be formed in any direction required by exciting the actuators in specific order with different time delays. The directed beam is a result of constructive wave interference.

To be able to predict the shape and direction of the main beam, as well as the unavoidable side lobes, the wave propagation from each transducer needs to be known. In an isotropic plate, omnidirectional point sources can be generally assumed with amplitude and velocity equal in every direction. Using this assumption, Yu and

Giurgiutiu have developed a general beamforming algorithm for a 1D linear phased array applied to an isotropic plate using a delay and sum principle (2007b; ?). The algorithm was also applied and validated with experiments.

Other phased array setups, such as rectangular and circular organization of the actuators, have also been suggested and explored by other researchers (Yu & Giurgiutiu, 2007a; Wilcox, 2003). Many cases have produced more optimal beamforming, e.g. large and narrow main lobe and smaller side lobes, which are the most sought after qualities for effective beamsteering. Most of this research however has only been done in isotropic materials.

An omnidirectional point source cannot always be assumed and the previously mentioned beamforming algorithm developed by Yu and Giurgiutiu is not universally applicable even in isotropic plates, as shown by Kim and Philen for MacroFiber Composites (MFC) actuators that have anisotropic actuation (2008). When trying to apply the same beamforming principles to composite structures, similar complications occur due to the anisotropic properties.

As mentioned earlier, in each layer, the wave speed and direction are affected by the angle between the wave propagation and the fibers. Extra wave interactions also occur at each layer boundary and are a function of the angles between layers. Specific frequencies can be found in some cases for a particular mode where the slowness curve is nearly circular, and an omnidirectional source wave approximation is applicable. In such cases, a beamforming algorithm for isotropic materials can be applied, as shown by Yan and Rose (Yan & Rose, 2007).

For a general case, however, a single point source in composite laminates can not be assumed as omnidirectional. The wave mode velocities, as well as amplitudes are direction and frequency dependent. Consequently, the wave front is no longer circular and can become very complicated for certain wave modes.

## 1.4 Finite Element Analysis

When dealing with complex geometries, material properties or loads, it is often not possible to obtain analytical mathematical expressions for the solutions (Logan, 2007). Finite element analysis (FEA) is a numerical approach to determining approximate solutions for physical models without obtaining a complete analytical solution. It can be used for structural analysis, fluid flow, heat transfer and other areas. It has been shown by many researchers that FEA methods are effective at predicting and evaluating guided lamb wave propagation (Yang, Ye, Su, & Bannister, 2006; Gresil, Giurgiutiu, Shen, & Poddar, 2012)(Han, 2007;Yang, 2006; Gresil et al., 2012).

The finite element approach involves division (discretization) of the model of interest into geometrically simple components/elements of finite size. Elements are interconnected by common points (nodes), boundary lines and surfaces. Sets of simpler algebraic equations governing each element are then combined for the whole model and solved concurrently.

For structural analysis problems there are various possible approaches for FEA. A common method is the displacement(stiffness) technique. Here, displacements for each node of each element are used as unknowns and are expressed through equations

of equilibrium. The shared nodes between elements result in systems of equations that need to be solved simultaneously to obtain a final solution. Alternative approaches include the principle of minimum potential energy and the principle of virtual work.

There are many commercially available computer finite element programs. In this thesis, Abaqus 6.14-1 program suite is used. ABAQUS includes two distinct solvers for dynamic problems, Abaqus/Standard and Abaqus/Explicit.

Abaqus/Standard employs an implicit time integration approach to calculate the transient response of the model. This method solves a set of dynamic equilibrium equations at every time increment using an iterative process. This is an unconditionally stable approach regardless of the time step, but can be very computationally and memory intensive.

Abaqus/Explicit uses an explicit central-difference time stepping integration technique. This method calculates the solution at every time step from the kinematic state at the end of previous step without iterations ("ABAQUS 6.14 User Manual", 2014). Therefore the solution can become unstable and begin propagating an increasingly large error if the time step is too large. This means it is only conditionally stable; however, it is much more computationally efficient for transient problems such as wave propagation ("ABAQUS 6.14 User Manual", 2014).

## 2. Guided Lamb Waves

Lamb waves, also known as guided waves, are elastic waves propagating in solid plates. Their motion is guided by the physical plate boundaries, which is acknowledged by using the prefix 'guided' lamb waves. The initial mathematical analysis and prediction of these types of waves in infinite plates was conducted and published in 1917 by Horace Lamb, after whom they are named. Similar guided waves were shown to exist on the surface of semi-infinite solids by Lord Rayleigh in 1885. Due to many similarities, the two wave types are often referred to in conjunction as Rayleigh-Lamb waves. Lamb wave theory has also been extended to curved plates, shells and pipes. The rest of the chapter will be limited to the problem as applied to simple plates.

Schematic of the problem and adopted notation are shown in Figure 2.1. The $x_3$ axis is defined parallel to the plate surface while $x_1$ and $x_2$ lie in-plane and further correspond to the primary material coordinate system in the anisotropic case. Guided lamb waves are characterized by the particle motion in the plane parallel to the plate normal and to the propagating direction, e.g. $x_1 - x_3$ plane for a wave traveling in $x_1$ direction.

A significant property of guided Lamb waves is the large number of possible wave modes for a given structure. A semi-infinite medium only supports two bulk wave modes types. These are dilatational (longitudinal/P-waves) and distortional (shear/S-

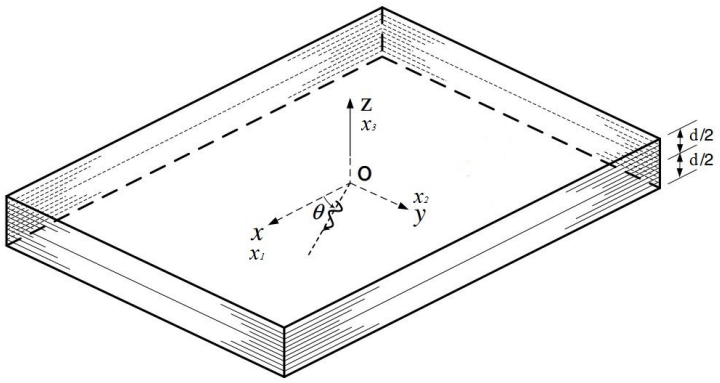


Figure 2.1. Plate model and notation

waves). Conversely, a finite plate can support an infinite number of Lamb wave modes, with ever more modes possible concurrently at increasing frequencies.

The motion of Lamb waves can be predicted from the general wave equation as shown in subsequent sections. In any medium, Lamb waves exhibit dispersion of phase and group velocity with frequency to a varying degree amongst different wave modes. Phase and group velocity concepts are further described in section 2.1 Generally, the Lamb wave modes can be classified into two groups, namely symmetric and antisymmetric (asymmetric). The two terms refer to the out-of plane component of particle motion in respect to the mid-plane as illustrated in Figure 2.2.

The actual particle motion is not constrained to the out-of plane displacement but is in fact elliptical. Asymmetric modes exhibit a larger component in the transverse $x_3$ direction, while symmetric modes tend to have a larger component parallel to the wave propagation direction. This is most significant for the primary zero-order modes. These characteristics lead to alternative names for the two classes of wave

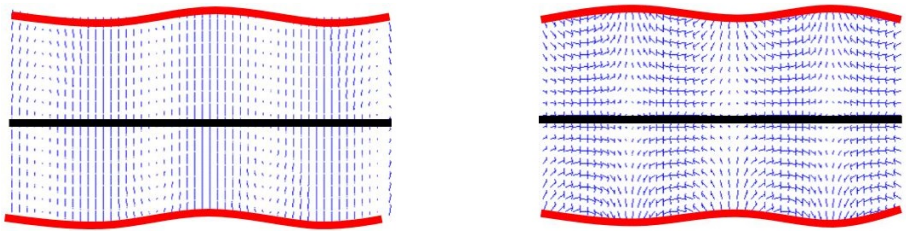

Figure 2.2. Out of Plane particle motion for Guided Lamb Waves (left - antisymmetric, right - symmetric)

modes - extensional for the symmetric and flexural for the antisymmetric. The following sections describe additional concepts regarding guided waves in more detail and present the governing equations of Lamb waves in isotropic and anisotropic plates as derived from 3D Elasticity Theory.

## 2.1 Phase and group velocities

As a group of waves travels through a medium, two distinct velocities can be distinguished. Group velocity is the velocity with which the entire envelope of the wave moves through the medium. Therefore it is the velocity of the progressing wavefront. Phase velocity on the other hand, is the velocity at which the individual wave peaks move. Amongst the first to note the distinction was Lord Rayleigh (1945):

> It has often been remarked that when a group waves advances into still water, the velocity of the group is less than that of the individual waves of which it is composed; the waves appear to advance through the group, dying away as they approach its interior limit. (p.475)

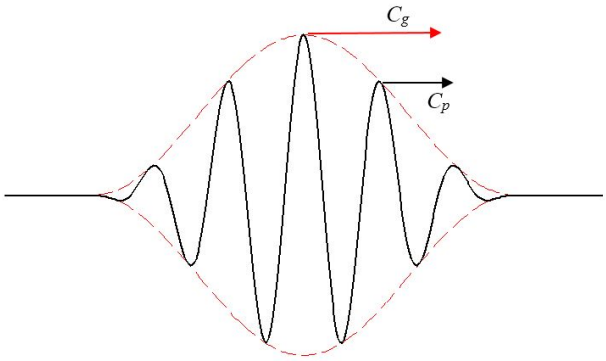


Figure 2.3. Phase ($C_p$) and group ($C_g$) velocities of a wave packet

In general, three distinct cases are possible. If phase and group velocity are equal, the wave peaks are stationary within the wave packet. If the phase velocity is greater, the waves seem to repeatedly originate at the beginning of the wave packet, traveling through it, and disappearing at the front. Finally, if the phase velocity is lower than group velocity, the waves seem to originate at the wavefront and travel opposite the propagation direction, vanishing at the beginning of the wave packet.

Any one of these cases can occur in guided Lamb waves. Both velocities depend on the material properties, plate thickness and the specific wave. Furthermore, they are both dispersive and vary throughout the frequency range for each wave mode. Derivations of the phase and group velocities governing equations is presented in the following sections.

## 2.2 Dispersion Curves

Dispersion curves describe the relation between the frequency and velocity for the different modes. The term 'dispersion' stems from the fact that both phase and group

velocity of any specific mode vary with frequency, and consequently a wave packet traveling through the plate appears to spread out, due to the different frequency components propagating at their own respective velocities. A sample of dispersion relations in an aluminum plate is shown in Figure 2.4.

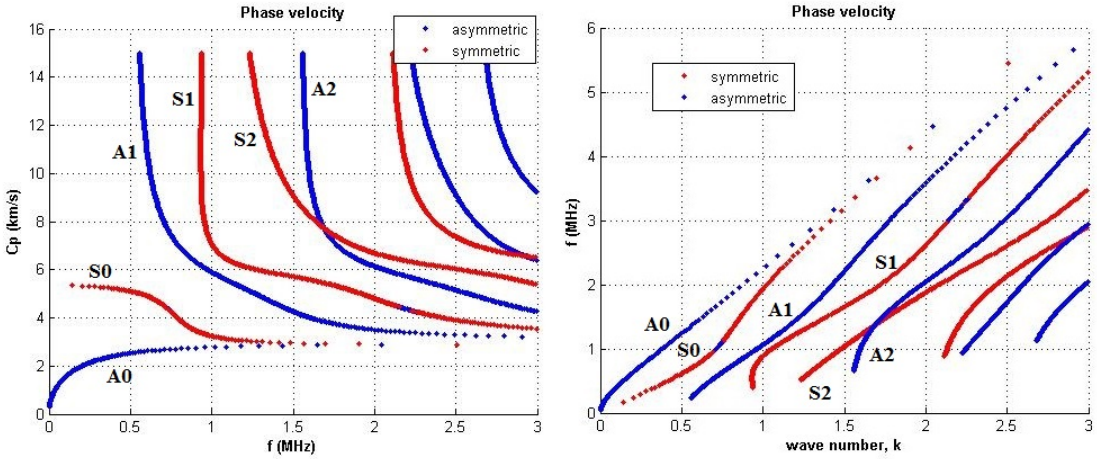


Figure 2.4. Dispersion relations in Al plate. Left: frequency - phase velocity representation; Right: Wavenumber - frequency representation

Dispersion relations for an isotropic plate are only a function of material properties and quite straightforward to derive from 3D elasticity theory. In the case of composite material however, guided wave propagation becomes more complex.

The number of layers, relations between layers themselves and angle between propagating waves and the fiber directions all affect the speed and amplitude of the wave propagation. Thus, all these factors affect dispersion, and the dispersion curve becomes different for various wave directions. Finally, the distinct wave modes

described earlier no longer exist clearly in composites and can be highly coupled in some directions, while uncoupled in others.

## 2.3 Wave curves

In anisotropic plates, due the previously described factors, the direction of the wave propagation has an affect on both phase and group velocity. This is due to differing material properties and consequently different stiffness matrices in various propagating directions $\theta$.

This effect is observed by plotting various 'wave curves' in a polar coordinate system. A plot of phase velocity vectors for different wave directions, $\theta$, for a specific plate at a certain frequency is called a (phase) velocity curve. A reciprocal of $1/C_p$ and the corresponding plot of values is called a slowness curve. Finally, a plot of group velocity vectors on polar plot is known as a wave curve. It can be shown that the group velocity vector for every point on the slowness curve is perpendicular to the tangent of the slowness curve at that point. The angle difference between the phase velocity vector and corresponding group velocity vector is denoted as a 'skew' angle. This phenomenon only occurs in anisotropic materials. The physical meaning of the skew angle is the direction of wave energy.

A wave curve essentially represents the shape of a wave front emitting from a single source at the origin. The mentioned phase velocity, slowness and wave curves for an isotropic material such as aluminum are simply circles, with varying magnitudes at different frequencies and wave modes; in composites however, the forms can become

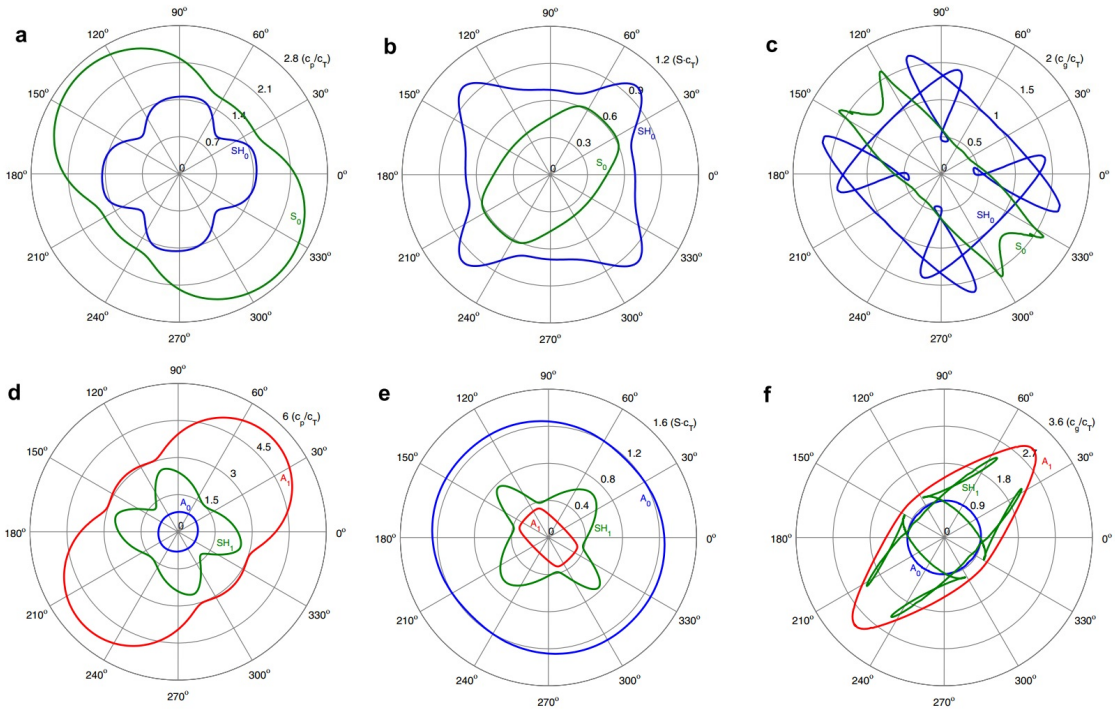


Figure 2.5. Velocity, slowness and wave curves of Lamb waves in $[+45_6/-45_6]_s$ laminate at $\omega hc_t = 4$: (a) velocity curves of symmetric modes; (b) slowness curves of symmetric modes; (c) wave curves of symmetric modes; (d) velocity curves of antisymmetric modes; (e) slowness curves of antisymmetric modes; (f) wave curves of antisymmetric modes; (Wang, 2004)

quite complicated. A sample of wave curves as published in literature for a 3mm thick $[+45_6/-45_6]_s$ composite laminate at a frequency of 0.4MHz is shown in Figure 2.5 (Wang, 2004). While certain wave modes, such as A0 in this example, might exhibit nearly isotropic properties, this is not always the case as seen from other wave modes. Furthermore, the A0 mode will also exhibit higher effects of anisotropy in the same plate at different frequencies.

## 2.4 Isotropic Material

### 2.4.1 Governing Equation Derivation

Derivation of elastic wave propagation governing equations in isotropic materials is presented in many textbooks (Graff, 1991; Nayfeh, 1995; Rokhlin, Chimenti, & Nagy, 2011; Rose, 1999). The derivation starts from the Navier elasticity equation for an isotropic and linearly elastic material:

$$(\lambda + 2\mu)\,\nabla\,(\nabla \cdot u) - \mu\nabla \times (\nabla \times u) = \rho\ddot{u} \tag{2.1}$$

where $\lambda$ and $\mu$ are Lamè constants. Expression in (2.1) represents a set of partial differential equations for displacements. Boundary conditions for the problem are free traction at both top and bottom surface of the plate, and are expressed by:

$$\sigma_{31} = \sigma_{32} = \sigma_{33} = 0 \quad @ \quad x_3 = \pm d/2 \tag{2.2}$$

Using method of potentials, equation (2.1) results in two expressions using Helmholtz decomposition ($u = \nabla\phi + \nabla \times \rho$):

$$\frac{\delta^2\phi}{\delta {x_1}^2} + \frac{\delta^2\phi}{\delta {x_3}^2} = \frac{1}{{c_L}^2}\frac{\delta^2\phi}{\delta t^2} \tag{2.3a}$$

$$\frac{\delta^2\psi}{\delta {x_1}^2} + \frac{\delta^2\psi}{\delta {x_3}^2} = \frac{1}{{c_T}^2}\frac{\delta^2\psi}{\delta t^2} \tag{2.3b}$$

Assuming solutions to (2.3) in the form of harmonic waves in $x_1 - x_2$ plane:

$$\phi = \phi(x_3)e^{i(\xi_1 x_1 + \xi_2 x_2 - \omega t)} \tag{2.4a}$$

$$\psi = \psi(x_3)e^{i(\xi_1 x_1 + \xi_2 x_2 - \omega t)} \tag{2.4b}$$

where $\xi_i$ is wavenumber in $i$ direction and $\omega$ is angular frequency. Through mathematical manipulation (Rose, 1999), two decoupled governing equations relating wavenumber and frequency for guided wave modes can be obtained:

$$\frac{\tan(qh)}{\tan(ph)} = -\frac{4k^2pq}{(q^2-k^2)^2} \qquad \text{symmetric modes} \tag{2.5}$$

$$\frac{\tan(qh)}{\tan(ph)} = -\frac{(q^2-k^2)^2}{4k^2pq} \qquad \text{antisymmetric modes} \tag{2.6}$$

where $p$ and $q$ terms are defined as follows:

$$p^2 = \frac{\omega^2}{{c_L}^2} - k^2 \tag{2.7a}$$

$$q^2 = \frac{\omega^2}{{c_T}^2} - k^2 \tag{2.7b}$$

### 2.4.2 Solving the Governing Equations

Dispersion relations for all possible wave modes are defined by the governing equations in (2.4.1). Valid solutions are the roots of the expression, and can be obtained by numerical methods. This produces a range of combinations of frequencies and phase velocities that correspond to valid guided wave modes. Steps taken in a typical solution approach are outlined by Rose (1999) as:

1. Choose a frequency-thickness product $(\omega h)_0$

2. Make an initial estimate of the phase velocity $(c_p)_0$

3. Evaluate the sign of the left-hand side of the governing equation

4. Choose another phase velocity $(c_p)_1 > (c_p)_0$ and re-evaluate the sign of governing equation.

5. Repeat steps 3 and 4 until the sign changes. Because the functions involved are continuous, a change in sign must be accompanied by a crossing through zero. Therefore, a root $m$ exist in the inverval where a sign change occurs. Assume that this happens between phase velocities $(c_p)_n$ and $(c_p)_{n+1}$.

6. Use some sort of iterative root-finding algorithm (e.g., Newton-Raphson, bisection,...) to locate precisely the phase velocity in the interval $(c_p)_n < c_p < (c_p)_{n+1}$ where the LHS of the governing equation is close enough to zero.

7. After finding the root, continue searching at this $\omega h$ for other roots according to steps 2 through 6.

8. Choose another $\omega h$ and repeat steps 2 through 7

The aforementioned steps can also be easily modified to solve the governing equations in the frequency-wavenumber domain instead of frequency-phase velocity, which can prove beneficial for mode-tracking (Lowe, 1995). In this case, a wavenumber is chosen and held constant, and then frequency (or frequency-thickness) is the iterative

variable. Once all the roots are found at a certain wavenumber, another wavenumber is chosen and steps are repeated.

## 2.5 Anisotropic Material Single Layer

Method of potentials presented in the isotropic material section can not be applied for an anisotropic material case, as starting equation (2.1) assumes isotropic properties. Therefore, the stress-strain relations that differ with direction in anisotropic materials need to be first evaluated, and then a partial wave method can be used to obtain a governing equation.

### 2.5.1 Stress-Strain relations

Composite materials are not only anisotropic, but also inhomogeneous by definition. The elastic constants are different and unique for fibers as well as for the matrix. However, when dealing with frequency at wavelengths that are large compared to characteristic dimensions such as lamina thickness, fiber diameter etc., it is the effective weighted average of properties that govern wave propagation (Rose, 1999). Therefore, composite materials can be modeled as homogeneous materials with effective elastic constants that are a function of both the fiber and matrix properties.

In a general case for a composite laminate there will be at least a single plane of symmetry, $x_1 - x_3$ plane, where $x_1$ is the $0^\circ$ fiber direction or principal material direction. Therefore the material stress-strain relations can be modeled as monoclinic.

For such a case, the stress-strain relations can be expressed with 13 independent constants:

$$\begin{Bmatrix} \sigma_{11} \\ \sigma_{22} \\ \sigma_{33} \\ \tau_{23} \\ \tau_{13} \\ \tau_{12} \end{Bmatrix} = \begin{bmatrix} C_{11} & C_{12} & C_{13} & 0 & 0 & C_{16} \\ C_{12} & C_{22} & C_{23} & 0 & 0 & C_{26} \\ C_{13} & C_{23} & C_{33} & 0 & 0 & C_{36} \\ 0 & 0 & 0 & C_{44} & C_{45} & 0 \\ 0 & 0 & 0 & C_{45} & C_{55} & 0 \\ C_{16} & C_{26} & C_{36} & 0 & 0 & C_{66} \end{bmatrix} \begin{Bmatrix} \epsilon_{11} \\ \epsilon_{22} \\ \epsilon_{33} \\ \gamma_{23} \\ \gamma_{13} \\ \gamma_{12} \end{Bmatrix} \tag{2.8}$$

For the sub-case of a unidirectional composite as well as for most composite layups in the primary material coordinates, two additional planes of symmetry can be defined. The system can then be modeled as orthotropic and represented with 9 independent constants:

$$\begin{Bmatrix} \sigma_{11} \\ \sigma_{22} \\ \sigma_{33} \\ \tau_{23} \\ \tau_{13} \\ \tau_{12} \end{Bmatrix} = \begin{bmatrix} C_{11} & C_{12} & C_{13} & 0 & 0 & 0 \\ C_{12} & C_{22} & C_{23} & 0 & 0 & 0 \\ C_{13} & C_{23} & C_{33} & 0 & 0 & 0 \\ 0 & 0 & 0 & C_{44} & 0 & 0 \\ 0 & 0 & 0 & 0 & C_{55} & 0 \\ 0 & 0 & 0 & 0 & 0 & C_{66} \end{bmatrix} \begin{Bmatrix} \epsilon_{11} \\ \epsilon_{22} \\ \epsilon_{33} \\ \gamma_{23} \\ \gamma_{13} \\ \gamma_{12} \end{Bmatrix} \tag{2.9}$$

$C_{ij}$ terms in equations (2.8) and (2.9) are stiffness constants and are a function of material properties - Young's moduli $E_i$, shear moduli $G_{ij}$ and Poisson ratios $\nu_{ij}$. Defining a common term:

$$\Delta = \frac{1 - \nu_{12}\nu_{21} - \nu_{23}\nu_{32} - \nu_{31}\nu_{13} - 2\nu_{21}\nu_{13}\nu_{32}}{E_1 E_2 E_3} \tag{2.10}$$

The elastic stiffness constants can be calculated as follows:

$$\begin{array}{lll} C_{11} = \frac{1-\nu_{23}\nu_{32}}{E_2E_3\Delta} & C_{12} = \frac{\nu_{21}+\nu_{31}\nu_{23}}{E_2E_3\Delta} & C_{13} = \frac{\nu_{31}+\nu_{21}\nu_{32}}{E_2E_3\Delta} \\ C_{22} = \frac{1-\nu_{13}\nu_{31}}{E_1E_3\Delta} & C_{23} = \frac{\nu_{32}+\nu_{12}\nu_{31}}{E_1E_3\Delta} & C_{33} = \frac{1-\nu_{12}\nu_{21}}{E_1E_2\Delta} \\ C_{44} = G_{23} & C_{55} = G_{13} & C_{66} = G_{12} \end{array} \tag{2.11}$$

To determine guided wave properties in a given propagating direction $\theta$ as measured from $x_1$ direction, the coordinate system needs to be rotated from the primary material coordinate system (where $x_1$ is the principal material direction or the 0° fiber direction) by $\theta$ around the $x_3$ axis. Denoting the constants in the primary coordinate system as $C'_{ij}$, the transformed stiffness constants $C_{ij}$ can be expressed as:

$$C_{ij} = [T(\theta)]^{-1} C'_{ij} \left([T(\theta)]^{-1}\right)^T \tag{2.12}$$

where $T$ is the transformation matrix and is defined as follows:

$$T(\theta) = \begin{bmatrix} \cos^2\theta & \sin^2\theta & 0 & 0 & 0 & 2\cos\theta\sin\theta \\ \sin^2\theta & \cos^2\theta & 0 & 0 & 0 & -2\cos\theta\sin\theta \\ 0 & 0 & 1 & 0 & 0 & 0 \\ 0 & 0 & 0 & \cos\theta & -\sin\theta & 0 \\ 0 & 0 & 0 & \sin\theta & cos\theta & 0 \\ -\cos\theta\sin\theta & \cos\theta\sin\theta & 0 & 0 & 0 & \cos^2\theta - \sin^2\theta \end{bmatrix} \tag{2.13}$$

### 2.5.2 Governing Equation Derivation

Starting from stress-strain relations in (2.8) and denoting the displacements in the 1/2/3 directions as $u_1, u_2$ and $u_3$, the strain components can be expressed as:

$$\begin{aligned} \epsilon_{11} &= \frac{\partial u_1}{\partial x_1} \qquad \gamma_{23} = \frac{\partial u_2}{\partial x_3} + \frac{\partial u_3}{\partial x_2} \\ \epsilon_{22} &= \frac{\partial u_2}{\partial x_2} \qquad \gamma_{13} = \frac{\partial u_1}{\partial x_3} + \frac{\partial u_3}{\partial x_1} \\ \epsilon_{33} &= \frac{\partial u_3}{\partial x_3} \qquad \gamma_{12} = \frac{\partial u_1}{\partial x_2} + \frac{\partial u_2}{\partial x_1} \end{aligned} \tag{2.14}$$

The governing equation of guided Lamb waves in a single layer can be derived from the equation of motion in an arbitrary medium:

$$\rho \frac{\partial^2 u_i}{\partial t^2} = \frac{\partial \sigma_{ij}}{\partial x_j} \tag{2.15}$$

where $i$ and $j = 1, 2, 3$. Assuming a solution to (2.15) in the form of a harmonic wave incident in the $x_1 - x_3$ plane:

$$u_i = U_i e^{i\xi(x_1 + \alpha x_3 - ct)} \tag{2.16}$$

where $\xi$ is the wavenumber in $x_1$ direction and $\alpha = \frac{\xi_3}{\xi}$ is the ratio of wavenumbers in $x_1$ and $x_3$ direction. Plugging (2.16) into (2.14), we obtain:

$$\begin{aligned} \epsilon_{11} &= \xi i U_1 e^{i\xi(x_1 + \alpha x_3 - ct)} \quad & \gamma_{23} &= \xi \alpha i U_2 e^{i(x_1 + \alpha x_3 - ct)} \\ \epsilon_{22} &= 0 & \gamma_{13} &= \xi \alpha i U_1 + \xi \alpha i U_3 e^{i(x_1 + \alpha x_3 - ct)} \\ \epsilon_{33} &= \xi i U_3 e^{i\xi(x_1 + \alpha x_3 - ct)} & \gamma_{23} &= \xi i U_2 e^{i(x_1 + \alpha x_3 - ct)} \end{aligned} \tag{2.17}$$

From which we can express the stress terms in (2.8) as:

$$\begin{aligned} \sigma_{11} &= \left[C_{11}U_1 + C_{13}\alpha U_3 + C_{16}U_2\right] i\xi e^{i\xi(x_1 + \alpha_3 - ct)} \\ \sigma_{22} &= \left[C_{12}U_1 + C_{23}\alpha U_3 + C_{26}U_2\right] i\xi e^{i\xi(x_1 + \alpha_3 - ct)} \\ \sigma_{33} &= \left[C_{13}U_1 + C_{33}\alpha U_3 + C_{36}U_2\right] i\xi e^{i\xi(x_1 + \alpha_3 - ct)} \\ \sigma_{23} &= \left[C_{44}\alpha U_2 + C_{45}\left(\alpha U_1 + U_3\right)\right] i\xi e^{i\xi(x_1 + \alpha_3 - ct)} \\ \sigma_{13} &= \left[C_{45}\alpha U_2 + C_{55}\left(\alpha U_1 + U_3\right)\right] i\xi e^{i\xi(x_1 + \alpha_3 - ct)} \\ \sigma_{12} &= \left[C_{16}U_1 + C_{36}\alpha U_3 + C_{66}U_2\right] i\xi e^{i\xi(x_1 + \alpha_3 - ct)} \end{aligned} \tag{2.18}$$

(2.15) can be expanded for each of the principal axis as:

$$\rho\frac{\partial^2 u_1}{\partial t^2} = \frac{\partial \sigma_{11}}{\partial x_1} + \frac{\partial \sigma_{12}}{\partial x_2} + \frac{\partial \sigma_{13}}{\partial x_3} \tag{2.19a}$$

$$\rho\frac{\partial^2 u_2}{\partial t^2} = \frac{\partial \sigma_{21}}{\partial x_1} + \frac{\partial \sigma_{22}}{\partial x_2} + \frac{\partial \sigma_{23}}{\partial x_3} \tag{2.19b}$$

$$\rho\frac{\partial^2 u_2}{\partial t^2} = \frac{\partial \sigma_{31}}{\partial x_1} + \frac{\partial \sigma_{32}}{\partial x_2} + \frac{\partial \sigma_{33}}{\partial x_3} \tag{2.19c}$$

where $\sigma_{13} = \sigma_{31}$; $\sigma_{23} = \sigma_{32}$ and $\sigma_{21} = \sigma_{12}$. Plugging (2.18) into (2.19) we obtain:

$$\left(C_{11} + C_{55}\alpha^2 - \rho c^2\right) U_1 + \left(C_{16} + C_{45}\alpha^2\right) U_2 + \left(C_{13}\alpha + C_{55}\alpha\right) U_3 = 0 \tag{2.20a}$$

$$\left(C_{16} + C_{45}\alpha^2\right) U_1 + \left(C_{66} + C_{44}\alpha^2 - \rho c^2\right) U_2 + \left(C_{36}\alpha + C_{45}\alpha\right) U_3 = 0 \tag{2.20b}$$

$$\left(C_{13}\alpha + C_{55}\alpha\right) U_1 + \left(C_{45} + C_{36}\alpha^2\right) U_2 + \left(C_{55} + C_{33}\alpha^2 - \rho c^2\right) U_3 = 0 \tag{2.20c}$$

Rewriting (2.20) in matrix form, where each $K_{ij}$ term is a function of material constants and $\alpha$:

$$\begin{bmatrix} K_{11} - \rho c^2 & K_{12} & K_{13} \\ K_{12} & K_{22} - \rho c^2 & K_{23} \\ K_{13} & K_{23} & K_{33} - \rho c^2 \end{bmatrix} \begin{Bmatrix} U_1 \\ U_2 \\ U_3 \end{Bmatrix} = 0 \tag{2.21}$$

Since $U_1 = U_2 = U_3 = 0$ is a trivial solution, the coefficient matrix needs to be singular, hence the determinant of (2.21) needs to equal 0:

$$\begin{vmatrix} K_{11} - \rho c^2 & K_{12} & K_{13} \\ K_{12} & K_{22} - \rho c^2 & K_{23} \\ K_{13} & K_{23} & K_{33} - \rho c^2 \end{vmatrix} = 0 \tag{2.22}$$

Solving (2.22) results in a sixth order polynomial in terms of $\alpha$:

$$\alpha^6 + C_1\alpha^4 + C_2\alpha^2 + C_3 = 0 \tag{2.23}$$

where $C_1$,$C_2$ and $C_3$ are factors in terms of material constants, $\rho$ and $c^2$. Solutions to (2.23) are in the form:

$$\alpha_1 = -\alpha_2 \qquad \alpha_3 = -\alpha_4 \qquad \alpha_5 = -\alpha_6 \tag{2.24}$$

Using relations in matrix (2.21) displacement ratios can be expressed:

$$V_q = \frac{U_{2q}}{U_{1q}} = \frac{K_{23}\left(K_{11} - \rho c^2\right) - K_{13}K_{12}}{K_{13}\left(K_{22} - \rho c^2\right) - K_{12}K_{23}} \tag{2.25a}$$

$$W_q = \frac{U_{3q}}{U_{1q}} = \frac{K_{23}\left(K_{11} - \rho c^2\right) - K_{13}K_{12}}{K_{12}\left(K_{33} - \rho c^2\right) - K_{13}K_{23}} \tag{2.25b}$$

Using above relations, the assumed solution in (2.16) can be expressed as:

$$\begin{bmatrix} u_1 \\ u_2 \\ u_3 \end{bmatrix} = \sum_{q=1}^{6} \begin{bmatrix} 1 \\ V_q \\ W_q \end{bmatrix} U_{1q} e^{i\xi(x_1 + \alpha x_3 - ct)} \tag{2.26}$$

And the stresses in (2.18) can be rewritten as:

$$\begin{aligned}
\sigma_{11} &= \sum_{q=1}^{6} \left[C_{11} + C_{16}V_q + C_{13}\alpha_q W_q\right] U_{1q} i\xi e^{i\xi(x_1 + \alpha_q x_3 - ct)} \\
\sigma_{22} &= \sum_{q=1}^{6} \left[C_{12} + C_{26}V_q + C_{23}\alpha_q W_q\right] U_{1q} i\xi e^{i\xi(x_1 + \alpha_q x_3 - ct)} \\
\sigma_{33} &= \sum_{q=1}^{6} \left[C_{13} + C_{36}V_q + C_{33}\alpha_q W_q\right] U_{1q} i\xi e^{i\xi(x_1 + \alpha_q x_3 - ct)} \\
\sigma_{23} &= \sum_{q=1}^{6} \left[C_{45}\alpha_q + C_{44}\alpha_q V_q + C_{45}W_q\right] U_{1q} i\xi e^{i\xi(x_1 + \alpha_q x_3 - ct)} \\
\sigma_{13} &= \sum_{q=1}^{6} \left[C_{55}\alpha_q + C_{45}\alpha_q V_q + C_{55}W_q\right] U_{1q} i\xi e^{i\xi(x_1 + \alpha_q x_3 - ct)} \\
\sigma_{12} &= \sum_{q=1}^{6} \left[C_{16} + C_{66}V_q + C_{46}\alpha_q W_q\right] U_{1q} i\xi e^{i\xi(x_1 + \alpha_q x_3 - ct)}
\end{aligned} \tag{2.27}$$

The traction free boundary conditions at the top and bottom surface of the lamina can be expressed as:

$$\sigma_{33} = \sigma_{23} = \sigma_{13} = 0 \quad @ \quad x_3 = \pm d/2 \tag{2.28}$$

Rewriting (2.27) in matrix form for the boundary conditions terms:

$$\begin{bmatrix} \sigma_{33} \\ \sigma_{23} \\ \sigma_{13} \end{bmatrix} = \sum_{q=1}^{6} i\xi \begin{bmatrix} D_{1q} \\ D_{2q} \\ D_{3q} \end{bmatrix} U_{1q} e^{i\xi(x_1 + \alpha x_3 - ct)} \tag{2.29}$$

where $D_{1q}, D_{2q}$ and $D_{3q}$ are:

$$\begin{bmatrix} D_{1q} \\ D_{2q} \\ D_{3q} \end{bmatrix} = \begin{bmatrix} C_{13} + C_{36}V_q + C_{33}\alpha_q W_q \\ C_{45}\alpha_q + C_{44}\alpha_q V_q + C_{45}W_q \\ C_{55}\alpha_q + C_{45}\alpha_q V_q + C_{55}W_q \end{bmatrix} \tag{2.30}$$

Evaluating (2.29) at the boundary conditions in (2.28) yields:

$$\begin{vmatrix} D_{11}E_1 & D_{12}E_2 & D_{13}E_3 & D_{14}E_4 & D_{15}E_5 & D_{16}E_6 \\ D_{21}E_1 & D_{22}E_2 & D_{23}E_3 & D_{24}E_4 & D_{25}E_5 & D_{26}E_6 \\ D_{31}E_1 & D_{32}E_2 & D_{33}E_3 & D_{34}E_4 & D_{35}E_5 & D_{36}E_6 \\ D_{11}\bar{E}_1 & D_{12}\bar{E}_2 & D_{13}\bar{E}_3 & D_{14}\bar{E}_4 & D_{15}\bar{E}_5 & D_{16}\bar{E}_6 \\ D_{21}\bar{E}_1 & D_{22}\bar{E}_2 & D_{23}\bar{E}_3 & D_{24}\bar{E}_4 & D_{25}\bar{E}_5 & D_{26}\bar{E}_6 \\ D_{31}\bar{E}_1 & D_{32}\bar{E}_2 & D_{33}\bar{E}_3 & D_{34}\bar{E}_4 & D_{35}\bar{E}_5 & D_{36}\bar{E}_6 \end{vmatrix} = 0 \tag{2.31}$$

where $E_q = i\xi e^{-i\xi\alpha_q d/2}$ and $\bar{E}_q = i\xi e^{i\xi\alpha_q d/2}$ for $q = 1...6$

Due to the properties of the roots of (2.23) described in (2.24), we can deduce the following properties:

$$\begin{array}{lll} D_{12} = D_{11} & D_{14} = D_{13} & D_{16} = D_{15} \\ D_{22} = -D_{21} & D_{24} = -D_{23} & D_{26} = -D_{25} \\ D_{32} = -D_{31} & D_{34} = -D_{33} & D_{36} = -D_{35} \end{array} \tag{2.32}$$

Using these relations, (2.31) can then be expressed as:

$$\begin{vmatrix} D_{11}E_1 & D_{11}E_2 & D_{13}E_3 & D_{13}E_4 & D_{15}E_5 & D_{15}E_6 \\ D_{21}E_1 & -D_{21}E_2 & D_{23}E_3 & -D_{23}E_4 & D_{25}E_5 & -D_{25}E_6 \\ D_{31}E_1 & -D_{31}E_2 & D_{33}E_3 & -D_{33}E_4 & D_{35}E_5 & -D_{35}E_6 \\ D_{11}\bar{E}_1 & D_{11}\bar{E}_2 & D_{13}\bar{E}_3 & D_{13}\bar{E}_4 & D_{15}\bar{E}_5 & D_{15}\bar{E}_6 \\ D_{21}\bar{E}_1 & -D_{21}\bar{E}_2 & D_{23}\bar{E}_3 & -D_{23}\bar{E}_4 & -D_{25}\bar{E}_5 & -D_{25}\bar{E}_6 \\ D_{31}\bar{E}_1 & -D_{31}\bar{E}_2 & D_{33}\bar{E}_3 & -D_{33}\bar{E}_4 & -D_{35}\bar{E}_5 & -D_{35}\bar{E}_6 \end{vmatrix} = 0 \qquad (2.33)$$

Through additional mathematical manipulation (Nayfeh, 1995) (2.33) can be further simplified and decoupled into two governing equations for symmetric and asymmetric modes respectively.:

$$D_{11}G_1 \cot(\gamma\alpha_1) - D_{13}G_3 \cot(\gamma\alpha_3) + D_{15}G_5 \cot(\gamma\alpha_5) = 0 \qquad \text{symmetric modes} \qquad (2.34a)$$

$$D_{11}G_1 \tan(\gamma\alpha_1) - D_{13}G_3 \tan(\gamma\alpha_3) + D_{15}G_5 \tan(\gamma\alpha_5) = 0 \quad \text{antisymmetric modes} \qquad (2.34b)$$

where

$$\begin{gathered} \gamma = \xi d/2 = \omega d/2c_P = \pi f d/c_P \\ G_1 = D_{23}D_{35} - D_{33}D_{25} \\ G_3 = D_{21}D_{35} - D_{31}D_{25} \\ G_5 = D_{21}D_{33} - D_{31}D_{23} \end{gathered} \qquad (2.35)$$

Roots of equations in (2.34) correspond to valid guided wave modes and can be solved by the steps outlined in section 2.4.2. Since the material properties vary with wave propagation angle, the process needs to be repeated over a range of propagating angles $\theta$.

## 2.6 Anisotropic Material Multiple Layer

The governing equations derived in section 2.5.2 only apply to a singe layer or for a unidirectional composite layup, where the material properties are not changing through the laminate thickness. For sufficiently large wavelengths, that are an order of magnitude larger than the laminate thickness, the layering has no discernible effect, and the laminate can be modeled with properties averaged across thickness (Rokhlin et al., 2011).

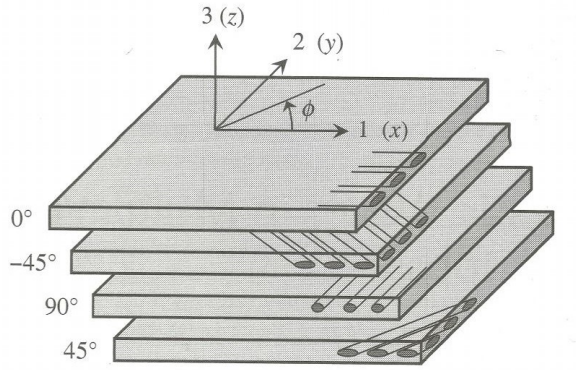


Figure 2.6. Schematic of a 4 layer [0/-45/90/45] composite laminate (Rokhlin, 2011)

For a general case of guided wave propagation and for most practical layups where multiple plies are stacked in the same orientation, the averaging approach is not suitable. To extend the theory to any composite layup, the set of governing equations needs to be solved for each layer and continuity at layer boundaries must be enforced. Schematic of the problem for a multi-layered composite plate is shown in Figure 2.6.

There are different approaches to formulating the multiple layer solutions, many of which adopt matrix methods. A thorough historical review of matrix techniques

for modeling wave propagation in multilayered media is given by Lowe (Lowe, 1995). A more recent overview including non-matrix methods is given by Kamal and Girguitiu (2014) who also propose a new stiffnes transfer matrix method for anisotropic composites.

A brief overview of popular methods is given in the following sections.

### 2.6.1 Transfer Matrix Method

The transfer matrix method (TMM) was first published by Thomson (1950) and combines the system of equations for each layer into six equations that relate the boundary conditions at the top and bottom of the plate. It doesn't solve for the displacement within each layer, which saves on computational time and complexity. It does however exhibit numerical instability at increasing frequency-thickness products due to combinations of very large and very small terms simultaneously (Lowe, 1995).

### 2.6.2 Global Matrix Method

The global matrix method was developed by Knopoff (1964). It includes stresses and displacements at each layer boundary with the top and bottom boundary conditions. This results in a single large matrix. It does not exhibit numerical instability, but becomes linearly larger and more computationally expensive as the number of layers increases.

### 2.6.3 Stiffness Transfer Matrix Method

The stiffness transfer matrix method (STMM) is a combined TMM and stiffness matrix method (SMM) developed by Kamal and Giurgiutiu (2014). The TMM method is unstable at higher frequencies as mentioned earlier. On the other hand, the SMM approach is unstable at lower frequencies but accurate elsewhere. STMM uses a combination of the two techniques to achieve numerical stability and robustness across the entire frequency range.

### 2.6.4 Higher Order Plate Theory

Higher order plate theory was shown by Wang (2004; 2007b) to accurately predict dispersion relations for symmetric and asymmetric modes at lower frequencies. Governing relations are developed by modifying Mindlin plate theory and including third order terms in the displacement expansion about the mid-plane. This approach is less computationally intensive but not applicable at large frequency-thickness products and for higher order modes (Wang, 2004).

### 2.6.5 Semi Analytical Finite Element

The semi-analytical finite element method (SAFE) is an alternative computationally efficient approach. It uses one dimensional finite element discretization through the thickness direction of the plate with 3 node elements. Derivation of dispersion relations using the SAFE method is shown by (Gao, 2007).

# 3. Phased Array Beamforming

Beamforming is a process of applying directionality to an array, either for signal transmission or reception. Also known as spatial filtering, it allows for spatial selectivity and amplification of the transmitted signal in the desired direction and suppression in other directions. If the direction of damage in relation to the array and time-of-flight data are both known, the exact location of damage can be pinpointed.

A beam is formed from constructive wave interference amongst multiple signals, while other directions are suppressed from destructive wave interference. Signals that arrive at a certain location in phase combine, while out of phase signals cancel out as shown in Figure 3.1. The beam in the target direction is referred to as the 'main lobe', while smaller beams that inevitably result in non-target directions are called 'side lobes'.

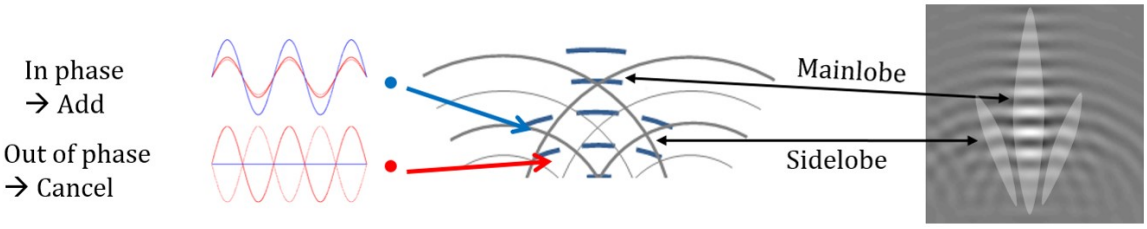


Figure 3.1. Beamforming through constructive and destructive wave interference

In certain cases, side lobes are at or close to the order of magnitude of the main lobe. These prominent lobes in non-desired directions are referred to as 'grating lobes'. The most desirable array response for structural health monitoring is a narrow main lobe, with small side lobes and no grating lobes. This allows for higher confidence in directional localization of damage.

The phased array approach achieves beamforming by using an array of actuators with a phase shift and/or different weights applied to the individual signals. With only a modest number of actuators, a focused beam can be formed in the desired direction, and thus damage localization becomes possible.

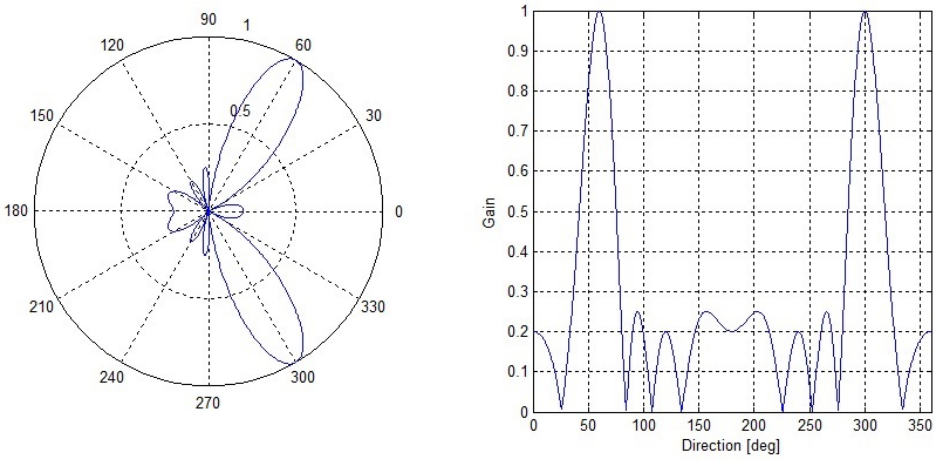


Figure 3.2. Directivity profile for a 5-actuator linear phased array in isotropic material, target angle 60°. Left - Polar plot representation; Right - Cartesian plot representation

Array performance or response is presented by a directivity profile which represents gain of the array as a function of signal direction. Array gain is typically normalized to a range of 0 to 1. The overall array response can be represented by

either a polar or cartesian plot of gain vs direction as shown in Figure 3.2. Polar plots will be used throughout the remainder of this thesis.

## 3.1 Near/Far field

It is important to note the distinction between near and far-field when evaluating phased array response. In far-field, wavefronts from a point excitation can be modeled as parallel planes and individual rays can be approximated as parallel(Yu & Giurgiutiu, 2007a). At ranges closer to the array, this approximation is no longer valid and this region is defined as the near-field. For a specific array, the condition can be expressed as:

$$\text{Near Field} < d_f < \text{Far Field} \tag{3.1}$$

where $d_f$ is the Fraunhofer distance. Defining $D$ as the overall array size and $\lambda$ as the wavelength of the signals, $d_f$ can be calculated as (Rudolph, 2013):

$$d_f = \frac{2D^2}{\lambda} \tag{3.2}$$

## 3.2 Beamforming equation for linear array in isotropic case

The combined response of the array can be mathematically represented as a summation of signals from all of the individual array elements. The wavefront from a single actuator at time $t$ and distance $\vec{r}$ from actuation can be expressed as a single tone radial wave:

$$f(\vec{r},t) = \frac{A}{\sqrt{r}} e^{j\left(\omega t - \vec{k}\vec{r}\right)} \tag{3.3}$$

where $A$ is amplitude, $\vec{k}$ is wave number and $\omega$ is angular frequency. A linear array of $M$ actuators as shown in Figure 3.3 is considered.

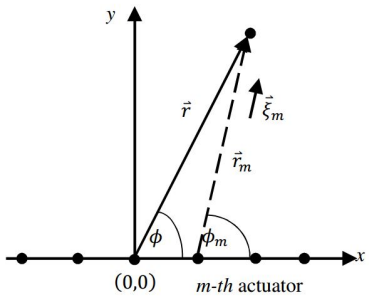


Figure 3.3. Schematic of a linear phased array and notations

If omnidirectional wave propagation with constant properties in all directions is assumed, the following expression for the response of a linear array can be obtained (Yu & Giurgiutiu, 2007b):

$$BF = \frac{1}{M} \sum_{m=0}^{M-1} \frac{w_m}{\sqrt{r_m/r}} e^{j\left[2\pi \frac{d}{\lambda} \frac{r}{d}\left(1 - \frac{r_m}{r} - \delta_m(\theta_0)\right)\right]} \tag{3.4}$$

where $d$ is the distance between the actuators, $w_m$ are weighting factors and $\delta_m$ are the time delays applied to $m$-th sensor to steer the beam in direction $\theta_0$.

Previous research has investigated linear phased arrays, and the $\frac{d}{\lambda}$ factor, where $d$ is the spacing between two actuators and $\lambda$ is the wavelength, was shown to have a significant effect on array performance. A value of 0.5 is optimal for most applications. Lower values result in wider main lobes in the target direction, while higher values can provide narrower main lobes but cause undesirable grating lobes in other directions.

These effects are shown for a 5 actuator linear array in Figure 3.4 for $\frac{d}{\lambda}$ values ranging from 0.3 to 0.7.

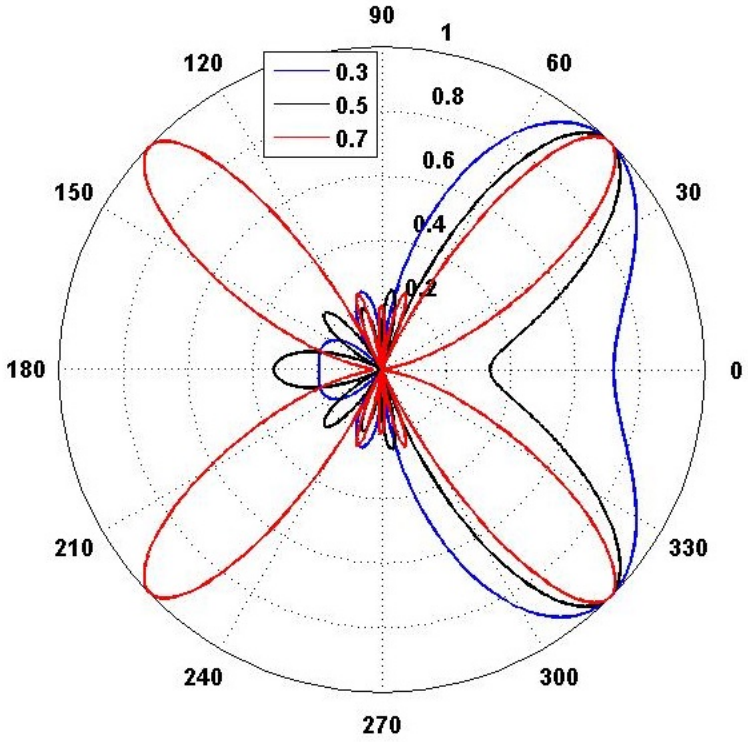


Figure 3.4. Effect of $\frac{d}{\lambda}$ on array beamforming properties for target angle of 45°

### 3.3 General beamforming algorithm for anisotropic case

Due to the anisotropic material properties of composite laminates, wavenumber, phase velocity and amplitude all vary with propagation direction $\theta$. Starting again from the wavefront expression for a single actuator, equation (3.3) needs to be modified as a function of propagation direction $\theta$:

$$f(\vec{r}, t, \theta) = \frac{A(\theta)}{\sqrt{r}} e^{j\left(\omega t - \vec{k}(\theta)\vec{r}\right)} \tag{3.5}$$

Using the same linear phased array setup as presented in Figure 3.3, a general delay and sum algorithm is derived. Using equation (3.5), summation of M signals from a linear array for a general anisotropic case can be expressed as:

$$z(\vec{r},t) = \sum_{m=0}^{M-1} w_m \frac{A(\theta)}{\sqrt{r_m}} e^{j\left(\omega t - \vec{k}_m(\theta)\vec{r}_m\right)} \tag{3.6}$$

where $w_m$ is a weight applied to $m$-th actuator. The exponential term in (3.6) can be rewritten as:

$$\begin{aligned} e^{j\left(\omega t - \vec{k}_m(\theta)\vec{r}_m\right)} &= e^{j\left(\omega t - (\vec{\xi}_m \frac{\omega}{c(\theta_m)})\vec{r}_m\right)} \\ &= e^{j\omega\left(t - \vec{\xi}_m \vec{r}_m \frac{1}{c(\theta_m)}\right)} \\ &= e^{j\omega\left(t - \frac{\vec{r}_m}{c(\theta_m)}\right)} \\ e^{j\omega\left(t - \frac{\vec{r}_m}{c(\theta_m)} + \left[\frac{r}{c(\theta)} - \frac{r}{c(\theta)}\right]\right)} &= e^{j\omega\left(\left(t - \frac{\vec{r}}{c(\theta)}\right) + \left(\frac{r}{c(\theta)} - \frac{r_m}{c(\theta_m)}\right)\right)} \\ e^{j\left(\omega t - \vec{k}_m(\theta)\vec{r}_m\right)} &= e^{j\left(\omega t - \vec{k}(\theta)\vec{r}\right)} e^{j\omega\left(\frac{r}{c(\theta)} - \frac{r_m}{c(\theta_m)}\right)} \end{aligned} \tag{3.7}$$

where $c(\theta)$ is the phase velocity magnitude in the $\theta$-direction and the $c(\theta)_m$ is the phase velocity from the $m$-th actuator to target. Using the term derived in (3.7), (3.6) becomes:

$$z(\vec{r},t) = \sum_{m=0}^{M-1} w_m \frac{A(\theta)}{\sqrt{r_m}} e^{j\left(\omega t - \vec{k}(\theta)\vec{r}\right)} e^{j\omega\left(\frac{r}{c(\theta)} - \frac{r_m}{c(\theta_m)}\right)} \tag{3.8}$$

Which can be further rewritten as

$$\begin{aligned} z(\vec{r},t) &= \sum_{m=0}^{M-1} w_m \frac{A(\theta)}{\sqrt{r_m}} \frac{\sqrt{r}}{\sqrt{r}} e^{j\left(\omega t - \vec{k}(\theta)\vec{r}\right)} e^{j\omega\left(\frac{r}{c(\theta)} - \frac{r_m}{c(\theta_m)}\right)} \\ &= \frac{A(\theta)}{\sqrt{r}} e^{j\left(\omega t - \vec{k}(\theta)\vec{r}\right)} \sum_{m=0}^{M-1} w_m \frac{1}{\sqrt{r_m/r}} e^{j\omega\left(\frac{r}{c(\theta)} - \frac{r_m}{c(\theta_m)}\right)} \end{aligned} \tag{3.9}$$

Therefore, (3.8) can be expressed as a multiplication of a single signal from the origin in (3.3) with a factor:

$$z(\vec{r},t) = f(\vec{r},t)\cdot BF \tag{3.10}$$

where $BF$ is the beamforming factor, which describes the combined array response gain as a function of direction and distance from the array's center.

$$BF = \sum_{m=0}^{M-1} w_m \frac{1}{\sqrt{r_m/r}} e^{j\omega\left(\frac{r}{c(\theta)} - \frac{r_m}{c(\theta_m)}\right)} \tag{3.11}$$

To form a beam aimed at distance r at angle $\theta_0$, the following time delays are introduced:

$$\delta_m(\theta_0) = \left(\frac{r}{c(\theta_0)} - \frac{r_m}{c(\theta_{m0})}\right) \tag{3.12}$$

The final beamforming factor expression, normalized by the number of actuators M, is then:

$$BF = BF(\theta, r, M) = \frac{1}{M}\sum_{m=0}^{M-1} w_m \frac{1}{\sqrt{r_m/r}} e^{j\omega\left(\frac{r}{c(\theta)} - \frac{r_m}{c(\theta_m)} - \delta_m(\theta_0)\right)} \tag{3.13}$$

For a target sufficiently far from the array, a far field model can be used. As explained in section 3.1, we can then use the following relation: $\theta \approx \theta_m$. When this approximation is valid, (3.13) can be simplified as:

$$BF = \frac{1}{M}\sum_{m=0}^{M-1} w_m \frac{1}{\sqrt{r_m/r}} e^{j\omega\left(\frac{r-r_m}{c(\theta)} - \delta_m(\theta_0)\right)} \tag{3.14}$$

And the corresponding time delays are:

$$\delta_m(\theta_0) = \left( \frac{r - r_m}{c(\theta_0)} \right) \tag{3.15}$$

### 3.4 Results

Equations (3.4) and (3.13) were modeled in MATLAB to compare and evaluate beamforming properties in anisotropic materials. Phase velocity curve data for different laminates was used as published by Wang (2004, 2007) and shown in Figure 2.5.

To evaluate and compare the performance of the anisotropic case response for different laminates and various modes against the isotropic response, other factors were held constant. These included the number of actuators, $d/\lambda$ and $r/d$ ratios.

A 10 actuator linear array was modeled in all cases. Spacing d between actuators was adjusted such that $d/\lambda$ was equal to 0.5. For the anisotropic case $\lambda_{ave}$, the average wavelength over all propagating directions, was used to determine the spacing. To avoid the influence of the $r/d$ term in all cases, target was set in far field, i.e. $r >> d$.

Predicted beamforming plots for $[+45_6/\text{-}45_6]_s$ and $[+45/\text{-}45/0/90]_s$ laminates when exciting all the actuators simultaneously are shown in Figure 3.5. The response of an isotropic case, which would correspond for an example to an aluminum plate is shown on all plots. Inherent beamforming of a 10 actuator array in the isotropic case produces a narrow main beam width orientated at 90° with a symmetric beam at 270°. In the case of the S0 mode for a $[+45_6/\text{-}45_6]_s$ composite laminate, with an anisotropic phase velocity curve, the main beam is instead oriented at 106° with a

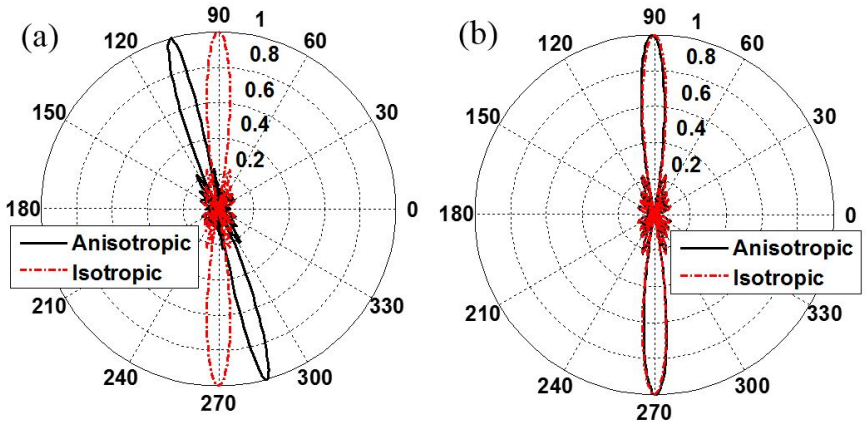


Figure 3.5. Inherent beamforming (no delays) of S0 mode with 10 actuator linear array. a) $[+45_6/\text{-}45_6]_s$ (b) $[+45/\text{-}45/0/90]_s$; isotropic response shown for comparison

second beam at 286°. Even for the S0 mode in the quasi-isotropic $[+45/\text{-}45/0/90]_s$ laminate with a seemingly isotropic phase velocity curve as shown in Figure 2.5, the main beam is still skewed slightly at 91°.

Once applying delays determined according to equation (3.12) to focus the beamforming in the 90 direction, results shown in Figure 3.6 are obtained. As seen in case (a) for the S0 mode in the $[+45_6/\text{-}45_6]_s$ laminate, a substantially narrower main lobe width is achieved compared to the isotropic case. However, a large undesirable grating lobe appears at 318° along with another prominent side lobe at 56°. On the other hand, in the case of the nearly isotropic mode in the second laminate in case (b), the main lobe is now aligned perfectly at 90° and exhibits almost identical performance to the isotropic case.

When steering the beam towards 135°, the anisotropic S0 mode in the $[+45_6/\text{-}45_6]_s$ laminate again achieves a narrower main lobe than the isotropic case, as shown

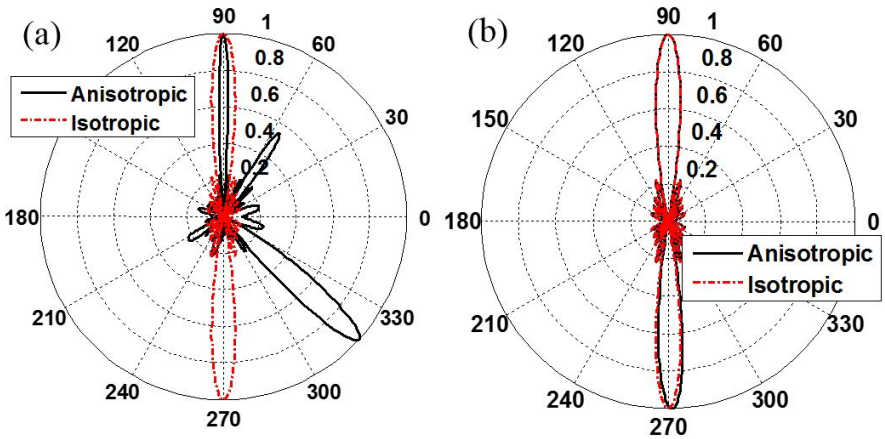


Figure 3.6. Beamforming of S0 mode with 10 actuator linear array with target angle 90°. a) $[+45_6/\text{-}45_6]_s$ (b) $[+45/\text{-}45/0/90]_s$; isotropic response shown for comparison

in Figure 3.7. The grating lobe at 270° is fairly narrow and much smaller than the symmetric grating lobe of the anisotropic case at 225°. In the case of the S0 mode in the $[+45_6/\text{-}45_6]_s$ laminate, a nearly identical response to the isotropic case is achieved.

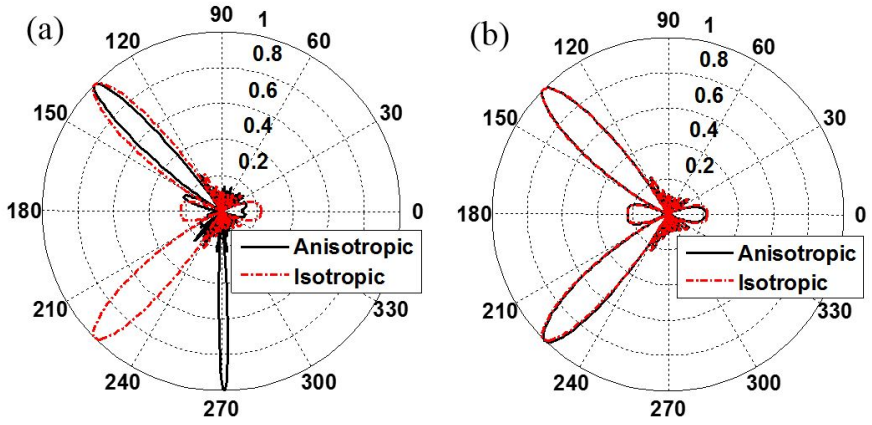


Figure 3.7. Beamforming of S0 mode with 10 actuator linear array with target angle 135. a) $[+45_6/\text{-}45_6]_s$ (b) $[+45/\text{-}45/0/90]_s$; isotropic response shown for comparison

The anisotropy is more prominent in certain directions than others, and may also cause beamsteering to fail. This is shown for a target direction of 50° and 40° in Figure 3.8. Beamforming for the S0 mode in the $[+45_6/-45_6]_s$ laminate fails as seen in (a). The main beam lobe is split at 50° and 62°. Furthermore, two prominent grating lobes are present at 86° and 333°. Beamsteering fails in a similar manner with a target angle of 40° as shown in (b). The splitting of the main beam lobes seems to be caused by the inflection point in the S0 phase velocity curve occurring at around 65° and 25° as seen in Figure 2.5 (a).

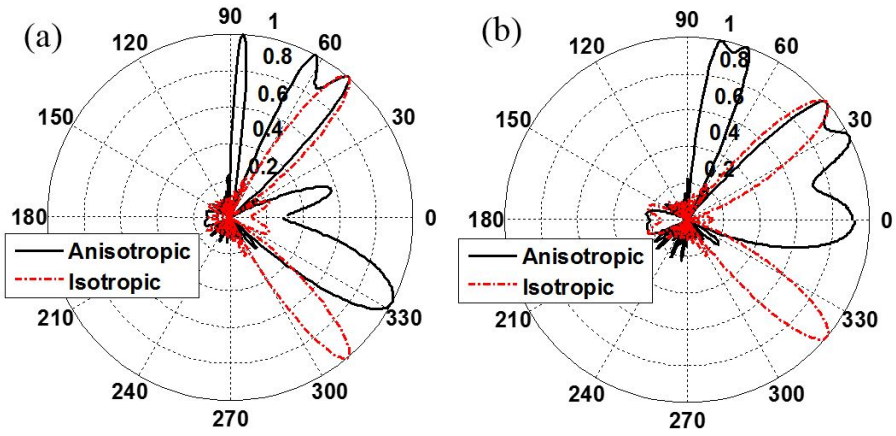


Figure 3.8. Beamforming of S0 mode with 10 actuator linear array in $[+45_6/-45_6]_s$ laminate. a) target angle 50° b) target angle 40°; isotropic response shown for comparison

By increasing the number of actuators M in a linear array, sidelobes can be effectively suppressed while the main beam lobe width is also decreased. Figure 3.9 shows the suppression of the sidelobe at 238° for the S0 mode in the $[+45_6/-45_6]_s$ laminate

with number of actuators varying between 4 and 16. However, the increasing number of actuators does not affect the amplitude of the grating lobe at 270°.

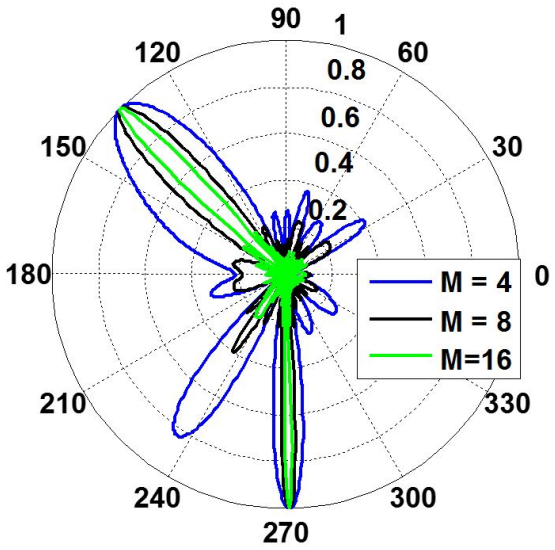


Figure 3.9. Beamforming of S0 mode with target angle 135° with varying number of actuators (M) for $[+45_6/\text{-}45_6]_s$ laminate

## 4. Finite Element Analysis and Discussion

Finite element model simulations were performed to compare to the phase array directivity profiles predicted by the general beamforming algorithm in equation (3.13). Abaqus 6.14-1 program suite was used for model creation, mesh generation, analysis and post processing.

Mesh resolution and time-step increment were chosen based on recommendations found in literature. As a general rule, mesh element size should be determined such that edge length is no greater than $1/10^{th}$ to $1/20^{th}$ of the shortest wavelength of interest to ensure a fine enough resolution (Sorohan et al, 2011; Gresil et al, 2012).

$$Ł_{max} = \frac{\lambda_{min}}{20} \tag{4.1}$$

Similarly, the time step needs to be chosen based on signal frequency such that there are at least 20 time steps per wave period (Gresil et al, 2012). Such a time step generally also satisfies the stability requirement limit as recommended in the Abaqus/Explicit user manual (2014).

$$\Delta t_{max} = \frac{1}{20f} \tag{4.2}$$

## 4.1 Model Set-up

Both isotropic and anisotropic plates were modeled to validate predictions of the beamforming algorithm. PZT actuators used in the experimental setup were modeled as concentrated nodal forces. Time displacement histories at nodes of interest were recorded for post-processing.

A fixed boundary condition was applied to all the plate edges for every model, and the total simulation time was chosen such as to prevent wave reflection from the plate edge boundaries to simplify data post-processing and focus only on the array performance.

### 4.1.1 Excitation Signal

A 2.5 Cycle Hanning windowed sine signal was used to excite guided wave propagation. A sample representative signal is shown in Figure 4.1. Hanning window was chosen due to its narrow band frequency content to minimize dispersion effects.

Excitation frequency was chosen based on dispersion relations such that only A0 and S0 modes would be present (i.e. below the cutoff frequency of higher modes). The excitation signals were then applied as concentrated nodal out-of-plane forces at actuator locations.

To achieve mode isolation, additional actuation nodes were specified at the bottom plane of the plate. When top and bottom nodes are excited using matching signals,

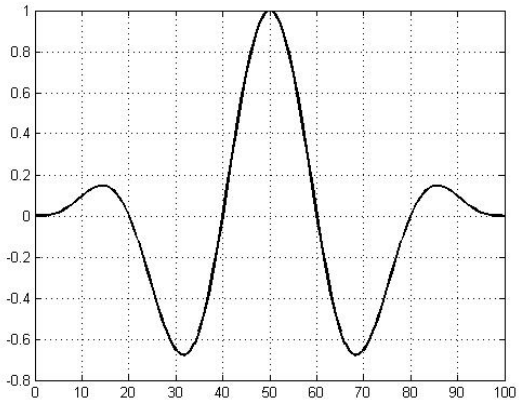


Figure 4.1. Typical 2.5 cycle Hanning signal used

symmetric modes can be isolated. If instead an inverse signal is applied to the other set of nodes, asymmetric modes are selectively excited.

### 4.1.2 Isotropic Plate Model

A 300x300x3mm 6061-T6 aluminum plate was modeled according to the physical plate used in the experimental setup. Material properties used are summarized in Table 4.1.

Table 4.1. Aluminum 6061-T6 material properties

| | | |
|---|---|---|
| **Density** ($\rho$) | 2700 | $kg/m^3$ |
| **Tensile Modulus** ($E$) | 68.9 | $GPa$ |
| **Possion Ratio** ($\nu$) | 0.33 | |

Dispersion relations of phase velocity for a 3mm thick Al plate are shown in Figure 4.2. Excitation was performed at a frequency of 0.05Mhz with a signal as shown in

Figure 4.1. At this frequency, only the fundamental asymmetric (A0) and symmetric (S0) modes exist.

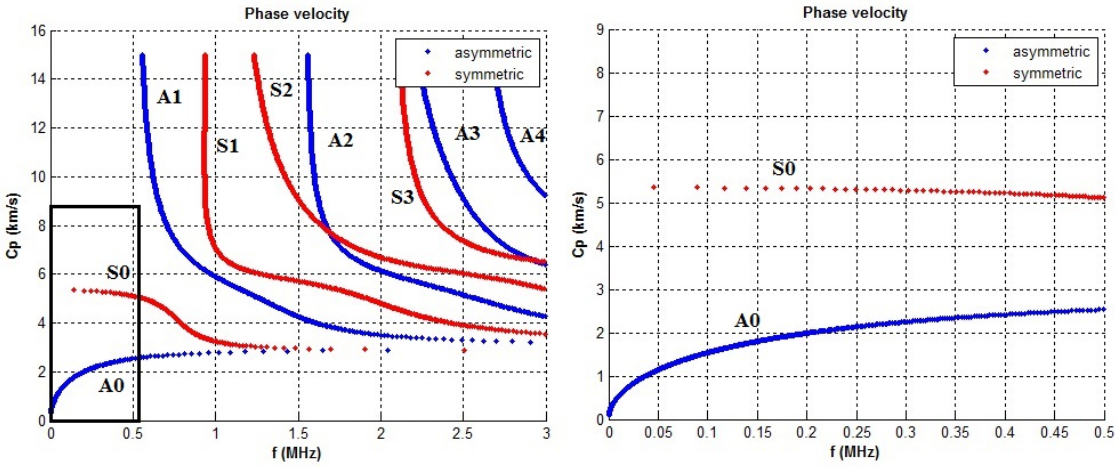


Figure 4.2. Phase velocity dispersion relations for 3mm thick Al Plate

The A0 mode was chosen for beamforming due to it's much larger out-of plane displacement component. At 0.05MHz in a 3mm thick Al plate, the A0 mode is expected with a group velocity of 2070m/s and phase velocity of 1140m/s, corresponding to a wavelength of 22.8mm. C3D8 elements were used to discretize the model. Mesh size and maximum time step were selected in accordance with guidelines described previously. All FEA model properties are summarized in Table 4.2.

Table 4.2. Isotropic Plate FEA model properties

| | |
|---|---|
| **Solver** | Abaqus/Explicit |
| **Element Type** | C3D8 |
| **Mesh Size** ($mm$) | 0.75 |
| **Maximum Time step** ($s$) | 1e-7 |
| **Total simulation time** ($s$) | 1e-4 |

A 5 actuator linear array was modeled in the center of the plate. Center-to-center distance between the actuators nodes was selected as $11.25mm$, resulting in a $\frac{d}{\lambda}$ value of 0.493. Sensor nodes were selected at a distance of $100mm$ from the center of the array, in 10° increments throughout the first quadrant. To capture the entire range of the array performance, a range of 180° on one side of the array should be monitored. Due to the inherent properties of a linear array, the response will always be symmetric across the array axis. The final FEA model with highlighted actuator and sensor nodes is shown in Figure 4.3.

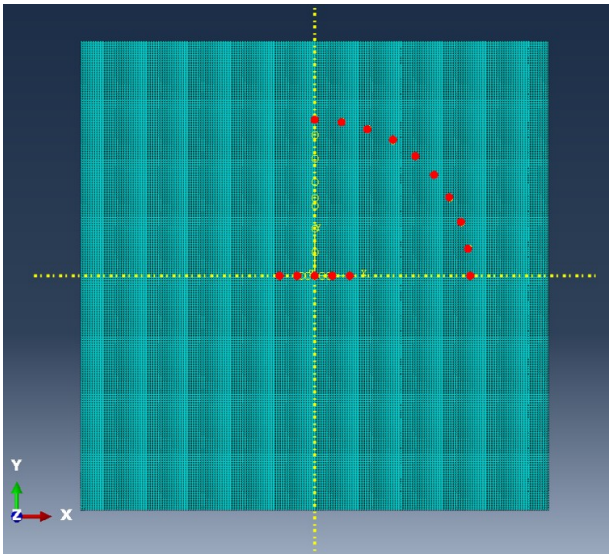


Figure 4.3. Aluminum Plate FEA model with actuator locations (5 red dots in x-axis) and sensor nodes in 10° increments

Fixed boundary condition was imposed along the side edges of the plate. Out-of-plane displacements according to the excitation signal described previously were introduced as concentrated force loads at the actuator locations. Time delays between the actuators were determined by Equation (3.12).

### 4.1.3 Anisotropic Plate Model

A 500x500x3mm 16ply unidirectional composite plate was modeled. Material properties were selected to represent pre-impregnated unidirectional composite with T700S fiber and Hankuk K1 at 36% resin content that was used in experimental validation. Material properties are summarized in Table 4.3.

Table 4.3. T700SC-12K/Hankuk K1 prepreg properties

| | | |
|---|---|---|
| $\rho$ | 1400 | $kg/m^3$ |
| $E_{11}$ | 127.0 | $GPa$ |
| $E_{22}$ | 8.1 | $GPa$ |
| $E_{33}$ | 8.1 | $GPa$ |
| $G_{23}$ | 3.5 | $GPa$ |
| $G_{13}$ | 5.2 | $GPa$ |
| $G_{13}$ | 5.2 | $GPa$ |
| $\nu_{23}$ | 0.458 | |
| $\nu_{13}$ | 0.248 | |
| $\nu_{12}$ | 0.248 | |

**Phase velocity Curve and Amplitude variation**

A single center point excitation model was first performed to determine the phase velocity curve and amplitude variation at 50kHz excitation. Sample dispersion relations for the modeled plate calculated from 3D elasticity theory and the governing equations presented in Section 2.5 are shown in Figure 4.4 for two different propagating directions. These plots include not only the Lamb wave modes but also shear-horizontal(SH) wave modes as they are also solutions to the governing equa-

tion. It can also be observed that only the primary modes exist at 50kHz for both propagating directions.

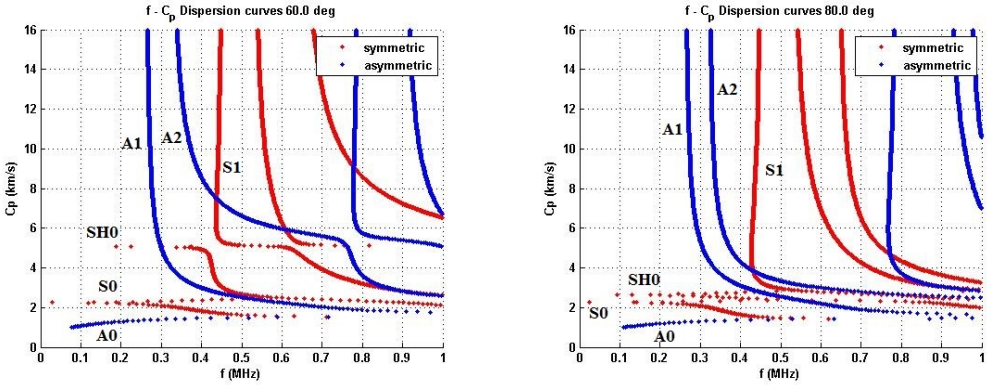


(a) (b)

Figure 4.4. Dispersion relations for phase velocity in 3mm thick unidirectional composite plate. (a) Propagating direction 60° (b) Propagating direction 80°

Signal was applied to top and bottom (inverse signal) of the plate to isolate the primary asymmetric mode - A0. Selective isolation of different modes for this case is shown in Figure 4.5.

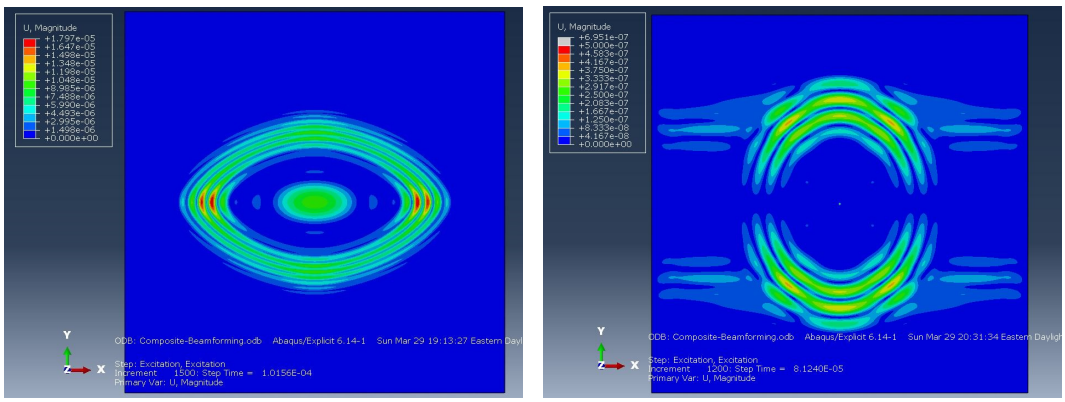


(a) (b)

Figure 4.5. Single source excitation in 3mm composite plate at 50kHz.(a) Isolated A0 mode (b) S0 mode and SH mode

Sensor nodes were selected at a distance of 100mm in 10° increments. In each direction, a second sensor node was specified a short distance (≈3mm) away. This setup is shown in Figure 4.6. Simulation settings are summarized in Table 4.4.

Table 4.4. Composite Plate FEA model properties

| | |
|---|---|
| **Solver** | Abaqus/Explicit |
| **Element Type** | C3D8 |
| **Mesh Size** ($mm$) | 0.75 |
| **Excitation Frequency** ($MHz$) | 0.005 |
| **Maximum Time step** ($s$) | 5e-7 |
| **Total simulation time** ($s$) | 1.5e-4 |

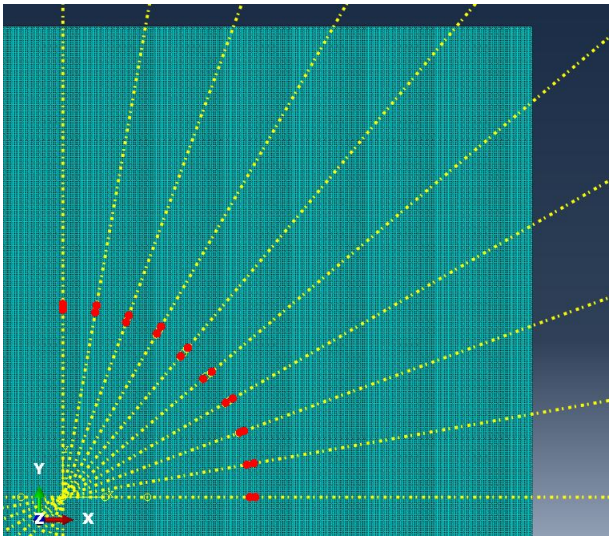


Figure 4.6. Composite Plate FEA model for Phase velocity curve determination

From out-of plane displacement history at two closely spaced points in same direction, phase velocity was determined based on the time difference of arrival of first major signal peak as shown in Figure 4.7 for a propagation direction 0°. This was then repeated for every propagation direction between 0° and 90°.

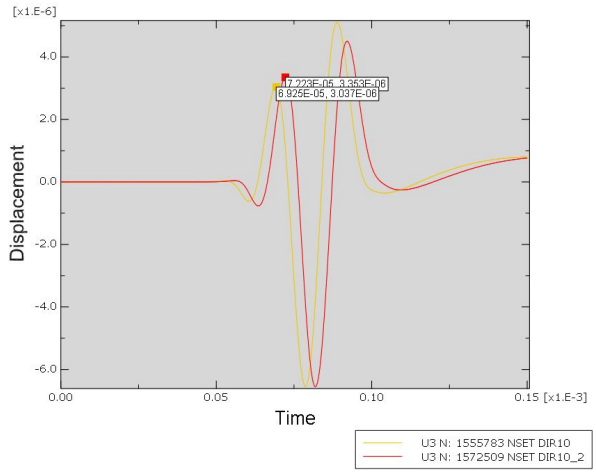


Figure 4.7. Phase velocity determination from two sensor nodes for direction 10°

Because this is a unidirectional laminate, wave curves for any mode will be symmetric across both the 0°and 90°axis. Therefore, taking measurements in one quadrant is sufficient and can be extrapolated to other directions. Results of phase velocity calculations for the A0 mode were curve fitted as an ellipse. The final phase velocity curve and corresponding slowness curve are shown in Figure 4.8.

Blue stars represent the results calculated from the FEA model, while the red dots represent results from 3D elasticity theory. The curve fit shown for phase velocity curve is expressed by equation (4.3).

$$c_p(\theta) = \frac{9.75e^5}{\sqrt{(750\cos(\theta))^2 + (1300\sin(\theta))^2}} \tag{4.3}$$

From the FEA model, amplitude variation with propagation direction $\theta$ was evaluated as well. Figure 4.9 shows the normalized amplitude in a given direction from a single source. Values were obtained by extracting the maximum signal value in each direction and normalizing to a scale of 0 to 1. The amplitude in the 0° direction was

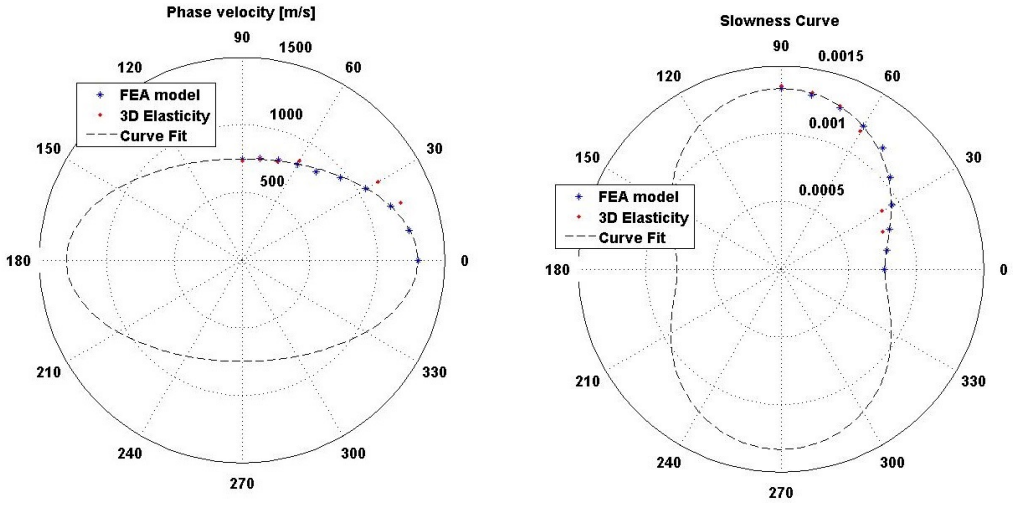


(a) (b)

Figure 4.8. Phase velocity and slowness curve for A0 mode at 50KHz in 3mm thick unidirectional composite laminate

observed to be significantly larger than 90° with another local maxima at approximately 45°. This amplitude variation needs to be multiplied with equation (3.13) to obtain the predicted beamforming performance of the array.

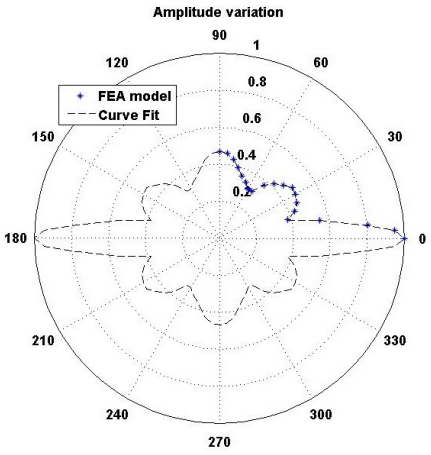


Figure 4.9. Amplitude variation with $\theta$ with single source excitation for A0 mode at 50KHz in 3mm unidirectional composite laminate

## 4.2 Isotropic Plate Beamforming

Three cases were evaluated for the isotropic case. The baseline case was inherent beamforming of the 5 actuator arrays, which is a result of no-time delays and simultaneous excitation of all actuators. Then, time delays were determined and applied according to Equation (3.12) to steer the beam in 70° and 45° directions. Using the center actuator as a reference, the time delays calculated from the algorithm are shown in Table 4.5.

The time histories of the out-of-plane displacements were recorded at each sensor node in the model. Maximum amplitudes in each direction were extracted and normalized to a scale from 0 to 1. These values were then compared to those predicted by the general beamforming algorithm in Equation (3.13).

Table 4.5. Isotropic Plate Time Delays

| | **Inherent** | **45°** | **70°** |
|---|---|---|---|
| **Actuator 1** $[s]$ | 0 | -1.49 E-05 | -8.55 E-06 |
| **Actuator 2** $[s]$ | 0 | -7.24 E-06 | -3.85 E-06 |
| **Actuator 3** $[s]$ | 0 | 0 | 0 |
| **Actuator 4** $[s]$ | 0 | 6.68 E-06 | 2.87 E-06 |
| **Actuator 5** $[s]$ | 0 | 1.26 E-05 | 4.65 E-06 |

Figure 4.10 is a result for inherent beamforming of the 5 actuator array with no time delays. The right side of the figure represents amplitudes obtained from the FEA model(red dots) overlaid on the prediction from the general beamforming algorithm.

Similarly, Figures 4.11 and 4.12 represent FEA results for beamforming with target directions 70° and 45°, respectively. In all cases, very good agreement is observed

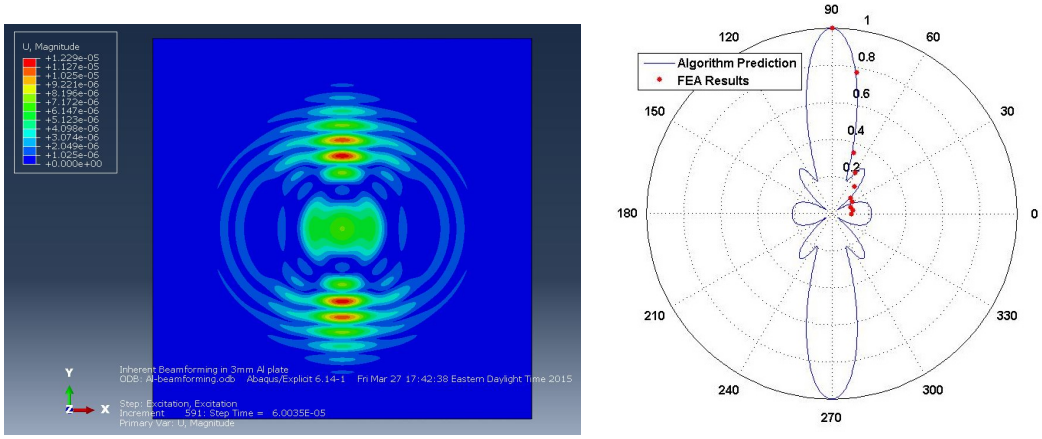


Figure 4.10. Inherent beamforming of 5 actuator array in isotropic plate

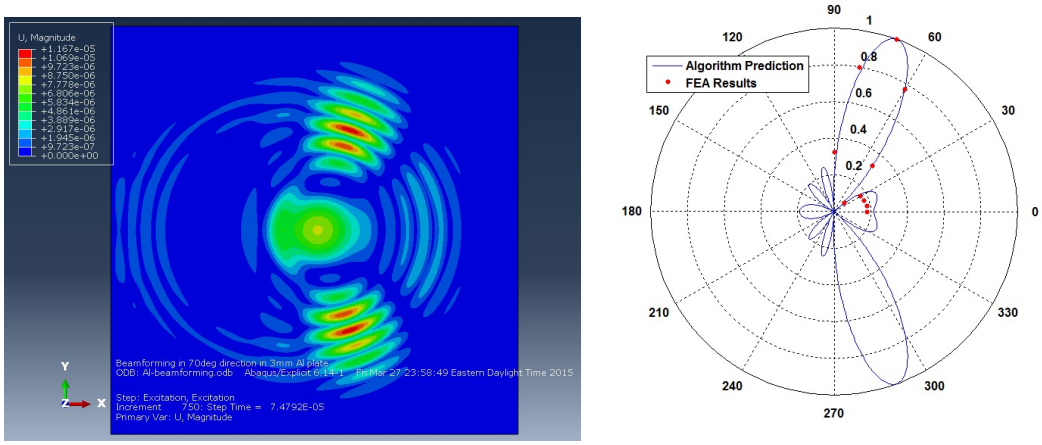


Figure 4.11. Beamforming in 70° direction with 5 actuator array in isotropic plate

between the algorithm prediction and the FEA results. Main beam width results are nearly identical. The 0°direction sidelobes in the inherent case and 70°case are present in the same locations as the algorithm predicts, but are smaller in magnitude.

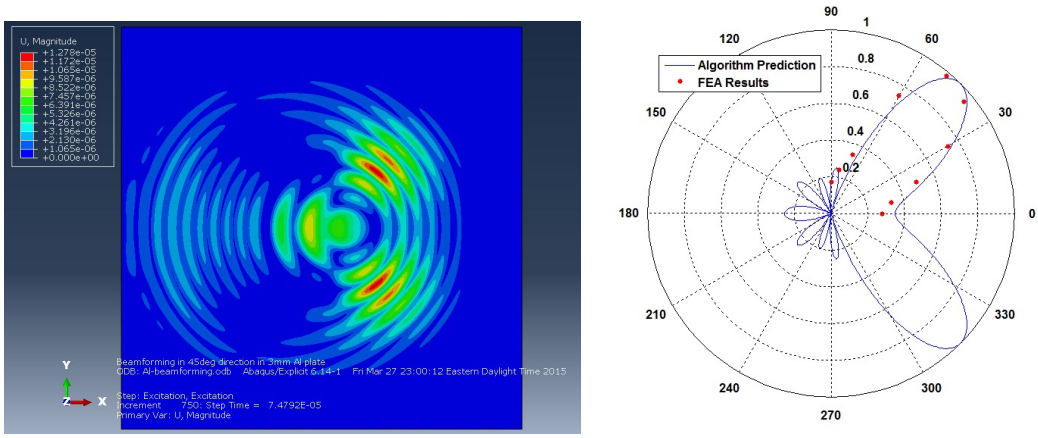


Figure 4.12. Beamforming in 45° direction with 5 actuator array in isotropic plate

## 4.3 Anisotropic Plate Beamforming

Three cases were evaluated for the anisotropic case, similarly as for the isotropic model. The aseline case was the inherent beamforming of a 5 actuator array when all actuators were excited concurrently. Actuator spacing was set to $9mm$ and held constant amongst the cases. 50kHz excitation was used in all cases. Time delays were determined and applied according to Equation (3.12) to steer the beam in 70° and 40° directions. Using the center actuator as a reference, the time delays calculated from the algorithm are shown in Table 4.6.

Time histories of the out-of-plane displacements were recorded at each sensor node in the model. Maximum amplitudes in each direction were extracted and normalized to a scale from 0 to 1. These values were then compared to those predicted by Equation (3.13) multiplied with the amplitude variation of a single source in Figure 4.9.

Table 4.6. Composite Plate Time Delays

| | **Inherent** | **40°** | **70°** |
|---|---|---|---|
| **Actuator 1** $[s]$ | 0 | -8.43E-06 | -3.55 E-06 |
| **Actuator 2** $[s]$ | 0 | -4.08E-06 | -1.60 E-06 |
| **Actuator 3** $[s]$ | 0 | 0 | 0 |
| **Actuator 4** $[s]$ | 0 | 3.76 E-06 | 1.24 E-06 |
| **Actuator 5** $[s]$ | 0 | 7.17 E-06 | 2.11 E-06 |

Figure 4.13 represents inherent beamforming of the 5 actuator array in the unidirectional composite plate when exciting all actuators simultaneously. The main lobe as determined from the FEA result is slightly narrower than the algorithm prediction, however, overall analytical predictions are a good match to the FEA results. The side lobe in the 0° direction is significantly larger than the comparable isotropic case in Figure 4.10, which is due to the high amplitude in the fiber direction from a single source.

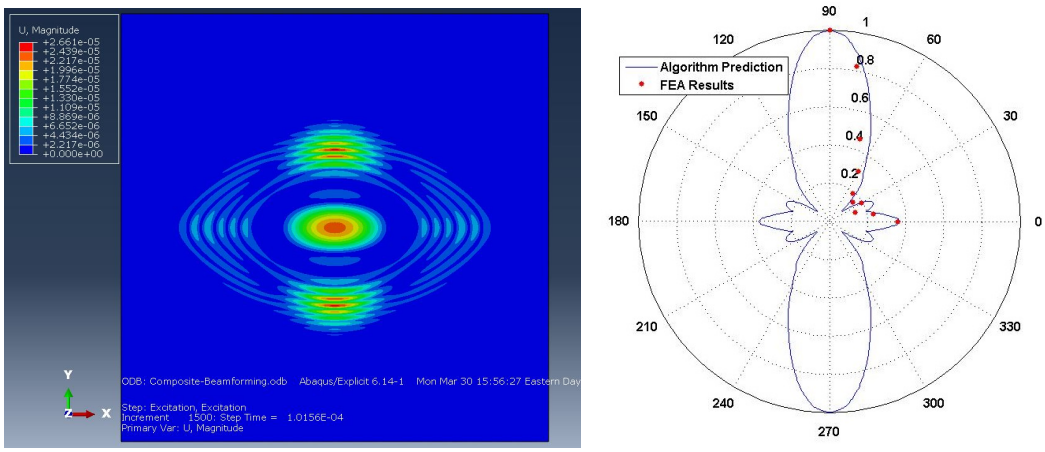


Figure 4.13. Inherent beamforming of 5 actuator array in Composite plate

Beamforming results for the 70° target direction are shown in Figure 4.14. While beamforming is successfully achieved, the main lobe is offset from the desired direction and is instead maximum at around 80°. This is due to the amplitude variation from every single actuator which is higher in 80°and close to a local minimum in the 70° direction. Another effect of the amplitude variation of every single source can be seen in the side lobe at 50° which is present in both the algorithm prediction and observed FEA results.

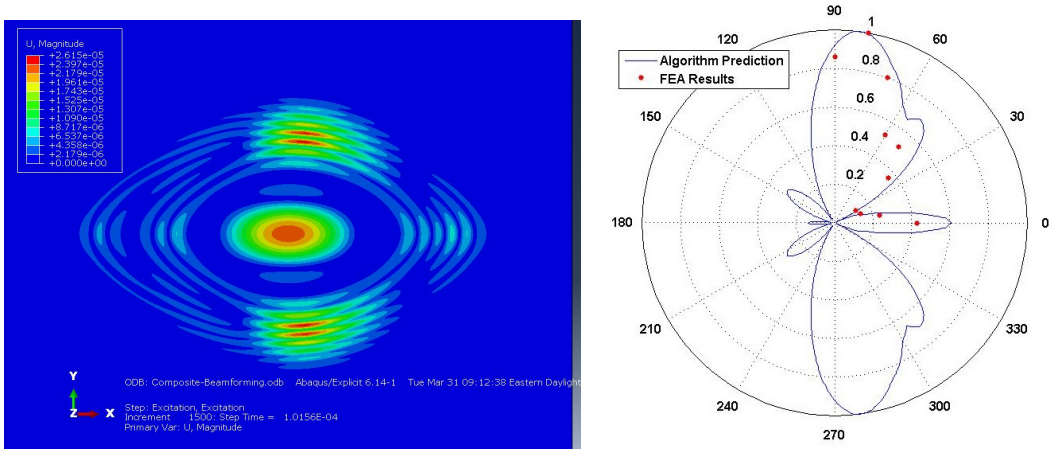


Figure 4.14. Beamforming in 70° with 5 actuator array in Composite plate

A comparison of the effect of amplitude variation on the algorithm predictions for a beam in the target direction of 70° is shown in Figure 4.15.

The left side of the figure shows the algorithm prediction without accounting for amplitude variation, while the right side of the figure shows the results when amplitude term is included. It can be readily observed that the offset of the main beam, side lobe in the 50° direction and a larger side-lobe in the 0° direction are all

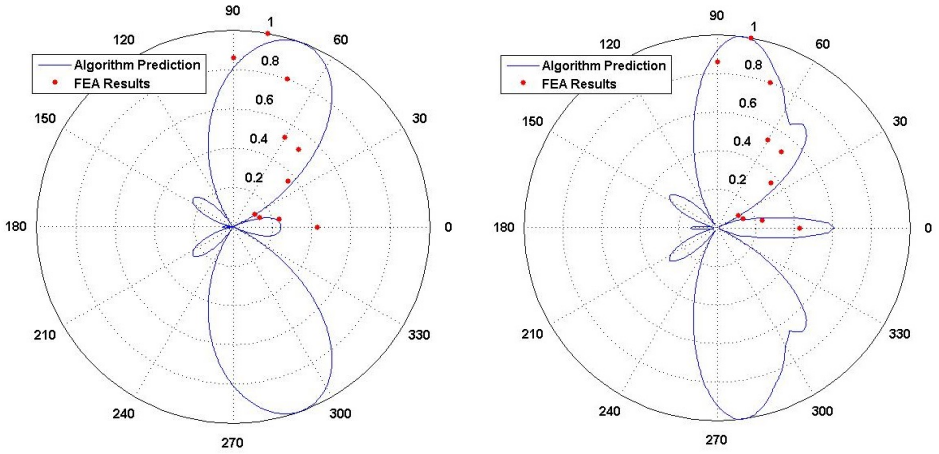


Figure 4.15. Effect of amplitude variation on predicted algorithm results and comparison to FEA results for beamforming in 70° direction

results of the inherent amplitude variation and correctly predicted by the algorithm when including amplitude variation.

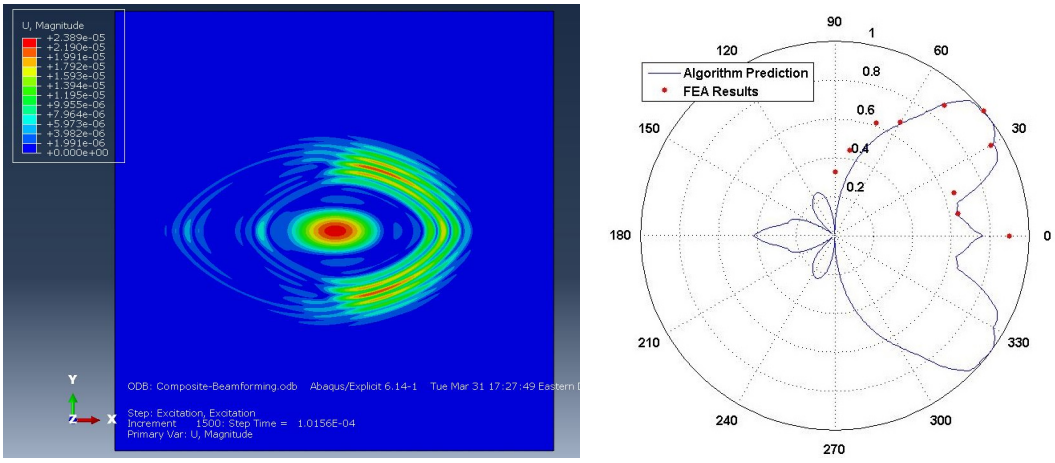


Figure 4.16. Beamforming in 40° with 5 actuator array in Composite plate

Beamforming results for the 40° target direction are shown in 4.16. Again, successful beamforming is achieved with the time delays determined by the algorithm. However, amplitude variation causes a grating lobe in the 0° direction combined with

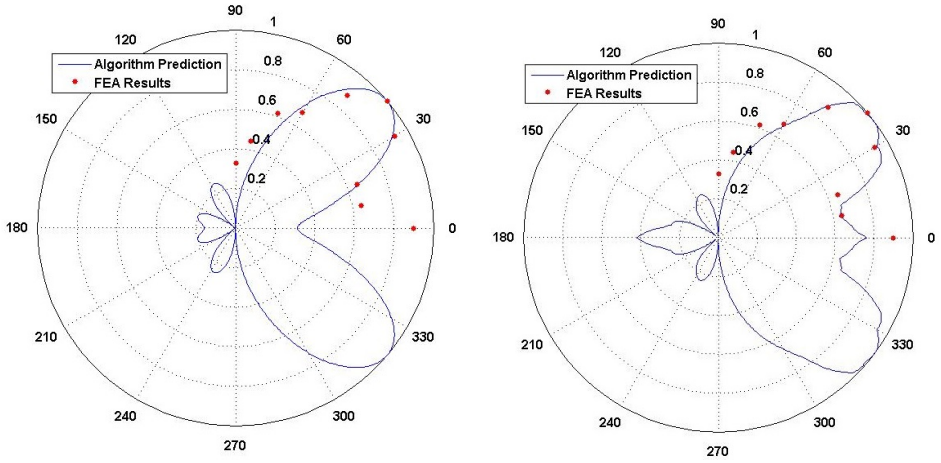


Figure 4.17. Effect of amplitude variation on predicted algorithm results and comparison to FEA results for beamforming in 40° direction

the main lobe. A comparison of the effect of amplitude variation on the beamforming results in shown in Figure 4.17.

A better match between FEA and analytical algorithm would likely be obtained if the sensors and target point were located further from the array. At a frequency of 50kHz and the given phase velocity curve for the A0 mode shown in Figure 4.7, the wavelength $\lambda$ varies between 30 and $52mm$ depending on direction. With a total array size of $36mm$, the distance for near/far field transition is between 86.4 and $49.8mm$, which does satisfy the far field approximations according to Equation (3.1). However, the near/far field classification does not account for the greatly varying amplitude with direction of each individual source and might have to be revised for the anisotropic case.

# 5. Experimental Validation

Experiments were performed on an aluminum and composite plate to validate both the FEA results and algorithm predictions. A 300x300x3mm 6061-T6 aluminum plate was used for the isotropic case. For the anisotropic case, an 8-layer unidirectional composite plate was manufactured using T700SC-12K/Hankuk K1 prepreg material.

The following sections describe the experimental setup and comparison of results for the FEA and algorithm predictions.

## 5.1 Experiment Setup

Piezoelectric (PZT) actuators were used to excite guided lamb waves. A 5 actuator linear array was used in all test cases with excitation applied only to top side of the plates. LabVIEW software was used with real-time FPGA hardware to precisely control the time delays for each actuator. A 2.5 cycle Hanning window excitation was used as described in the previous chapter. An amplifier was used to increase each channel's signal to improve measurement resolution. Depending on the case, 10-19 measurement points were used in the 1st quadrant in either 10° or 5° increments. A laser vibrometer was utilized to record out-of-plane velocities of the test plates at every measurement point. The complete experimental setup is shown in Figure 5.1.

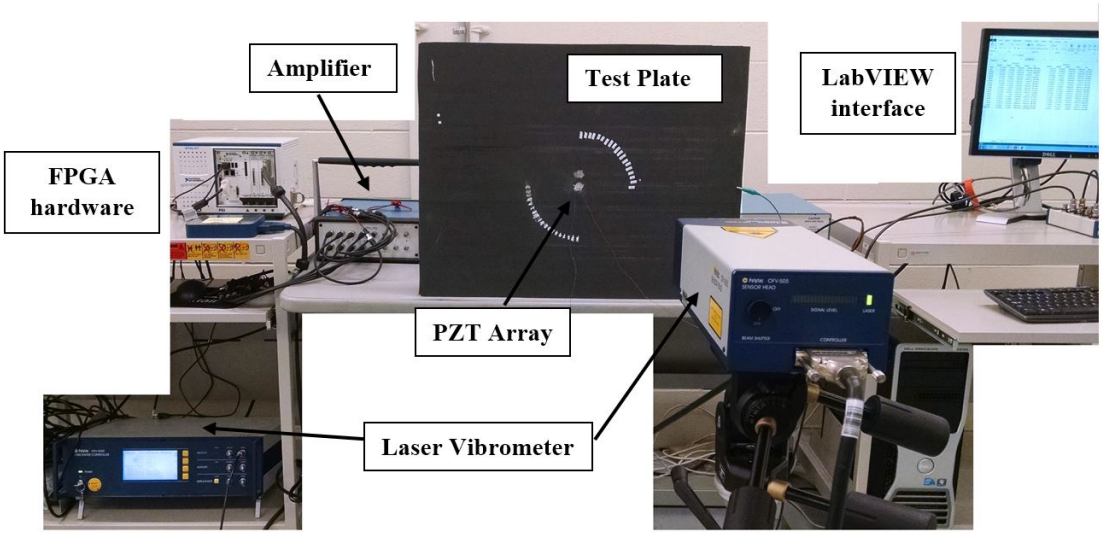


Figure 5.1. Experimental setup

The LabVIEW control software was set-up to perform 10 bursts at every measurement location to allow for averaging of results and noise-suppression. The output of the laser vibrometer recordings was post-processed with Matlab. Time-history vibration data at each measurement point was averaged for the 10 bursts. Low-frequency vibrations not associated with guided wave propagation were filtered out by removing linear trends in the data. Finally, averaged and detrended velocity history was integrated to obtain time-displacement history. An example of the vibrometer output and processed data is shown in Figure 5.2.

## 5.2 Phase Velocity and amplitude variaton measurement

Phase velocity measurements were performed in the same manner as described in Chapter 4 by tracking the wave peaks at two closely spaced measurement points. A

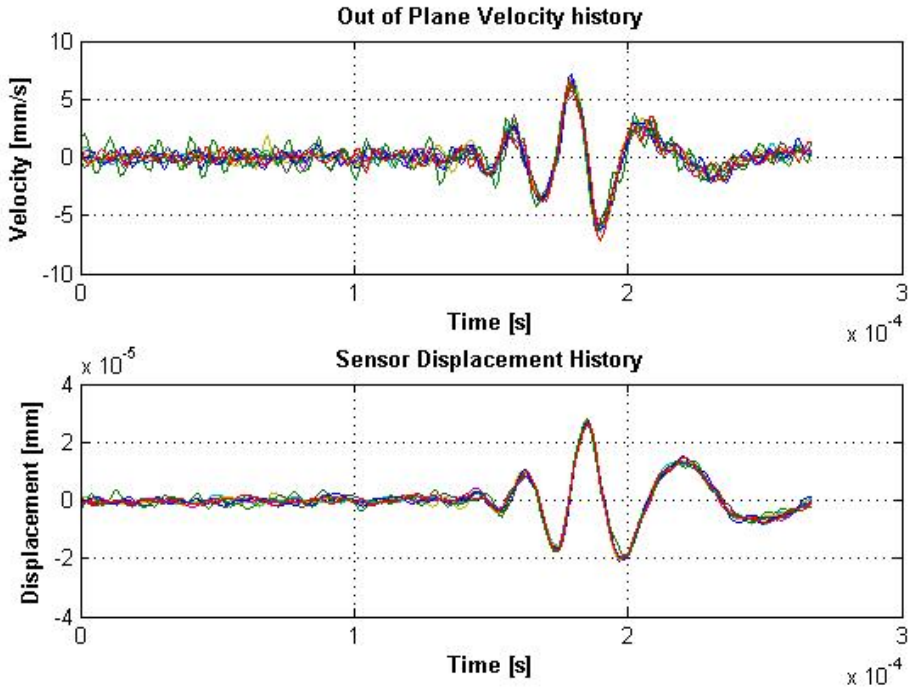


Figure 5.2. Sample vibrometer data and post processing

single central PZT was used for excitation. Phase velocity determination was first performed on the Aluminum plate at 50kHz to verify the experimental setup and approach. The results and comparison to both the 3D elasticity prediction and FEA results are shown in Table 5.1. Very good agreement is seen from all cases.

Table 5.1. Phase velocity of A0 mode at 50kHz in 3mm Aluminum 6061-T6 plate

| | | |
|---|---|---|
| **3D elasticity** | 1140 | $\frac{m}{s}$ |
| **FEA model** | 1162 | $\frac{m}{s}$ |
| **Experimental** | 1154 | $\frac{m}{s}$ |

Phase velocity was then also measured in the composite test plate to aid in the determination of time-delays for beamforming. Measurements were taken in 10° in-

crements in the first quadrant. Amplitude variation with propagating direction from a single source was also measured. Results for both phase velocity and amplitude variation are shown in Figure 5.3.

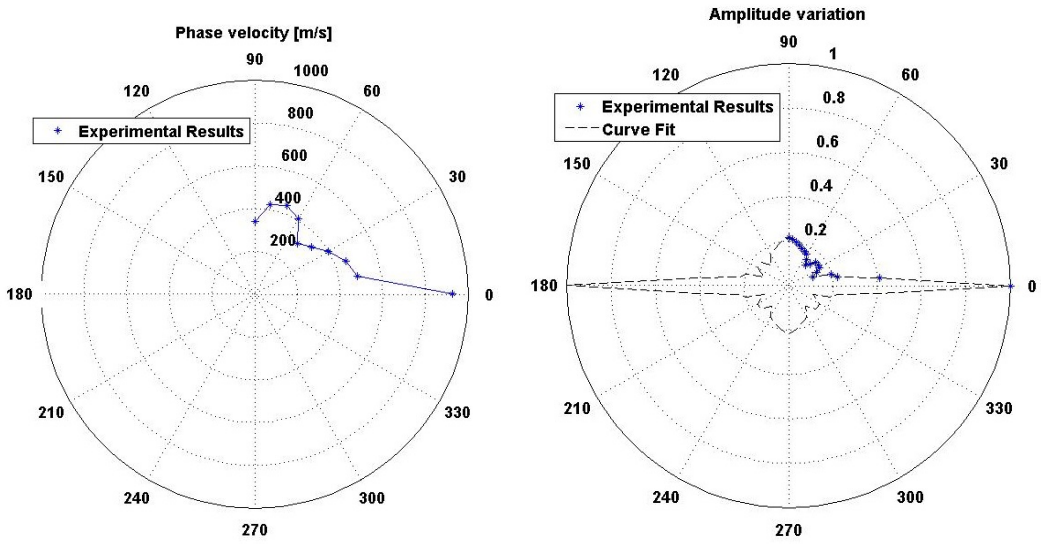


Figure 5.3. Single source excitation at 50kHz in Composite plate. Left - Phase velocity curve; Right - Amplitude variation with $\theta$

The amplitude variation exhibited a similar pattern as observed in the FEA model, however, an even higher maximum in the 0° direction was observed. The results for phase velocity variation were unexpected, as the FEA model and 3D elasticity theory indicated that it should follow an elliptical function, as seen in Chapter 4. This could be attributed to potential measurement error. The distance between the two measurement points had to be known very precisely, however it was very hard to achieve a focused laser point at an exact location using the vibrometer on the composite plate.

## 5.3 Validation of Numerical and FEA results

### 5.3.1 Isotropic Plate

For the Aluminum plate, two cases were experimentally evaluted - inherent beamforming with no time delays, and beamforming in 45° direction. The same time delays were used to steer the beam as in the FEA model, as the dimensions and frequency were the same. The cases and time delays are summarized in Table 5.2. The actuator spacing was same as in the FEA model as well, 11.25mm.

Table 5.2. Experiment Isotropic Plate Time Delays

| | **Inherent** | **45°** |
|---|---|---|
| **Actuator 1** $[s]$ | 0 | 0 |
| **Actuator 2** $[s]$ | 0 | 7.66 E-06 |
| **Actuator 3** $[s]$ | 0 | 14.90 E-06 |
| **Actuator 4** $[s]$ | 0 | 21.58 E-06 |
| **Actuator 5** $[s]$ | 0 | 27.50 E-06 |

Comparison of experimental results to algorithm prediction and FEA results for the inherent case and for beamforming in 45° direction is shown in Figures 5.4 and 5.5 respectively.

In both cases, a very good agreement between the algorithm prediction and experimental results was observed. A beam is successfully steered in the 45° direction in the 2nd case. Other beamforming properties such as width of the main lobe and locations of sidelobes are also in agreement amongst all approaches.

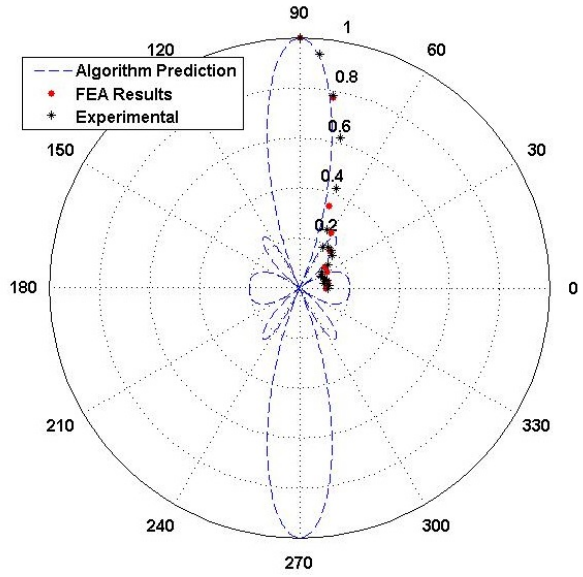


Figure 5.4. Inherent beamforming of 5-actuator array in Al plate - comparison of experimental results

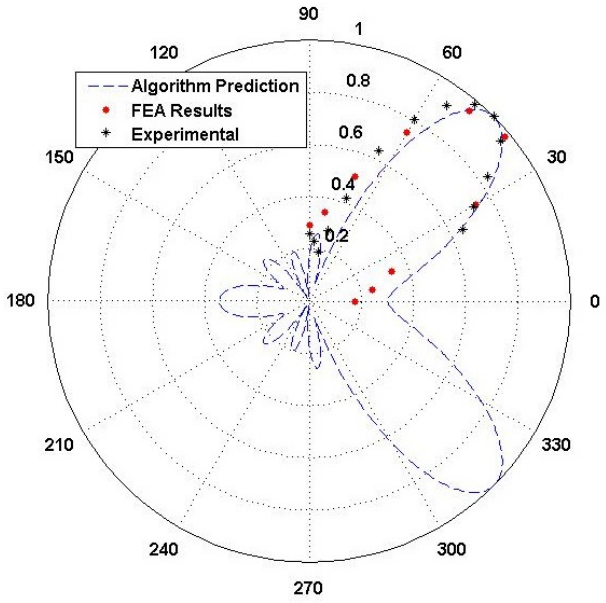


Figure 5.5. Beamforming in 45° direction of 5-actuator array in Al plate - comparison of experimental results

### 5.3.2 Anisotropic Plate

Three cases were experimentally evaluated for the composite plate - inherent beamforming of a 5-actuator array and beamsteering in 40° and 70° directions. The spacing between the actuators was set at 8.5mm. The summary of cases and time delays used is shown in Table 5.3.

Table 5.3. Experiment Composite Plate Time Delays

| | **Inherent** | **40°** | **70°** |
|---|---|---|---|
| **Actuator 1** $[s]$ | 0 | 0 | 0 |
| **Actuator 2** $[s]$ | 0 | 4.27 E-06 | 1.71 E-06 |
| **Actuator 3** $[s]$ | 0 | 8.18 E-06 | 3.11 E-06 |
| **Actuator 4** $[s]$ | 0 | 11.73 E-06 | 4.17 E-06 |
| **Actuator 5** $[s]$ | 0 | 14.89 E-06 | 4.92 E-06 |

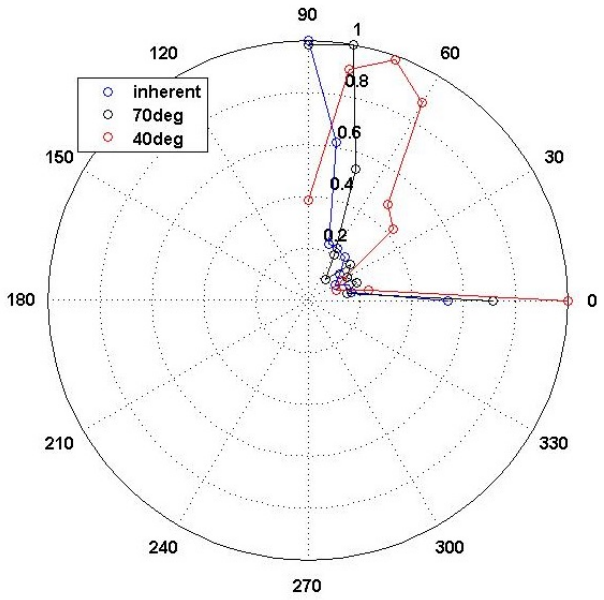


Figure 5.6. Experimental results for beamforming in unidirectional composite plate using a 5 actuator array

Experimental results for beamforming in the composite plate are shown in Figure 5.6. A successful beam was obtained in all cases, however not in the target directions. This is likely due to inaccuracies in the measurement of the phase velocity which was used to determine the time delays.

The 40° case exhibits a significant grating lobe in the 0° direction which can be attributed to the amplitude variation from a single source as described earlier. Still, the results indicate that it is possible to form a focused beam with a 5-actuator array in an anisotropic plate.

# 6. Conclusions and Recommendations

## 6.1 Summary

In this thesis, a general beam-forming algorithm is developed that accounts for non-omnidirectional guided wave propagation in anisotropic materials, namely composite laminates. The formulation accounts for variation of phase velocity with wave propagation angle and amplitude variation.

Using phase velocity curves for two different composite laminates determined from 3D elasticity, the beamforming properties of the general formulation with a linear phased array were examined. It is shown that even wave modes with highly anisotropic phase velocity profiles can result in good beam-forming characteristics in certain directions. Specifically, narrower main lobes are achieved with the same number of actuators as the baseline isotropic case. However, the effects of anisotropy cause the useful range of angles for effective beam-forming to be quite small, with large undesirable grating lobes created in other directions.

The predictions of the general beamforming algorithm are validated with finite element modeling for both the isotropic and anisotropic case. Good agreement is shown for both. Experimental validation is also performed. For an Aluminum plate, representative of an isotropic case, very good agreement is obtained between the algorithm prediction, FEA results and experimental results. For anisotropic case, using

a unidirectional composite plate, successful beamforming is obtained, however not in the desired directions. This is attributed to errors in phase velocity determination.

## 6.2 Recommendations and Future Work

Future work should focus on the study of amplitude variation from a single source in anisotropic plates and its effect on beamforming characteristics. Different 2D array designs should be investigated, as they could potentially enable robust beamforming capabilities in any desired direction. Applying different 'excitation weights'to specific actuators could also be explored to suppress the undesired beamforming properties due to anisotropy.

# REFERENCES


Abaqus 6.14 user manual [Computer software manual]. (2014). (Dassault Systemes)

Gao, H. (2007). *Ultrasonic guided wave mechanics for composite material structural health monitoring* (Unpublished doctoral dissertation). The Pennsylvania State University.

Graff, K. F. (1991). *Wave motion in elastic solid*. Dover Publications, Inc.

Gresil, M., Giurgiutiu, V., Shen, Y., & Poddar, B. (2012). Guidelines for using the finite element method for modeling guided lamb wave propagation in shm processes. In *6th european workshop on structural health monitoring.*

Kamal, A., & Giurgiutiu, V. (2014). Stiffness transfer matrix method (stmm) for stable dispersion curves solution in anisotropic composites. In *Proceedings of spie* (Vol. 9064).

Kim, D., & Philen, M. (2008). On the beamsteering characteristics of mfc phased arrays for structural health monitoring. In *49th aiaa/asme/asce/ahs/asc structures, structural dynamics, and materials conference.*

Knopoff, L. A. (1964). Matrix method for elastic wave problems. *Bulletin of the Seismological Society of America*, *54*, 431-438.

Lissenden, C., & Rose, J. (2008). Structural health monitoring of composite laminates through ultrasonic guided wave beam forming. In *Nato applied vehicle technology symposium on military platform ensured availability proceedings.*

Logan, D. L. (2007). *A first course in the finite element method* (4th ed.). Thomson.

Lowe, M. J. S. (1995). Matrix ttechnique for modeling ultrasonic waves in multilayered media. *IEEE Transactions on Ultrasonics, Ferroelectrics, and Frequency Control*, *42*(4), 525-541.

Nayfeh, A. H. (1995). *Wave propagation in layered anisotropic media: With application to composites*. North Holland.

Rayleigh, J. W. S. (1945). *Theory of sound*. New York: Dover.

Rokhlin, S. I., Chimenti, D. E., & Nagy, P. B. (2011). *Physical uultrasonic of composites*. Oxford University Press.

Rose, J. L. (1999). *Ultrasonic waves in solid media*. Cambridge University Press.

Rudolph, D. (2013). *Reduction of near-field grating lobes in sparse acoustic phased arrays* (Unpublished master's thesis). Embry-Riddle Aeronautical University.

Thomson, W. (1950). Transmission of elastic waves through a stratified solid medium. *Journal of Applied Pyhsics*, *21*, 89-93.

Valdes, S. H. D., & Soutis, C. (2002). Real-time nondestructive evaluation of fiber composite laminates using low-frequency lamb waves. *Journal of the Acoustical Society of America*, *111*, 2026-2033.

Wang, L. (2004). *Elastic wave propagation in composites and least-squares damage localization technique* (Unpublished master's thesis). Dept. Aerospace Engineering, North Carolina State University.

Wang, L., & Yuan, F. (2006). Experimental study of lamb wave propagation in composite laminates. In *Proceedings of spie.*

Wang, L., & Yuan, F. (2007a). Group velocity and characteristic wave curves of lamb waves in composites: Modeling and experiments. *Composites Science and Technology*, *67*, 1370-1384.

Wang, L., & Yuan, F. (2007b). Lamb wave propagation in composite laminates using a higher-order plate theory. In *Proceedings of spie.*

Wilcox, P. (2003, June). Omni-directional guided wave transducer arrays for the rapid inspection of large areas of plate structures. *EEE Transactions on Ultrasonics, Ferroelectrics, and Frequency Control*, *50*(6), 699 - 709.

Yan, F., & Rose, J. (2007). Guided wave phased array beam steering in composite plates. In *Proceedings of spie.*

Yang, C., Ye, L., Su, Z., & Bannister, M. (2006). Some aspects of numerical simulation for lamb wave propagation in composite laminates. *Composite Structures*, *75*, 267-275.

Yu, L., & Giurgiutiu, V. (2007a). In situ 2-d piezoelectric wafer active sensors arrays for guided wave damage detection. *Ultrasonics*, *48*(2), 117-134.

Yu, L., & Giurgiutiu, V. (2007b). In-situ optimized pwas phased arrays for lamb wave structural health monitoring. *Journal of Mechanics of Materials and Structures*, *2*(3), 459-487.